
The First VERA Astrometry Catalog

VERA collaboration, Tomoya HIROTA^{1,2}, Takumi NAGAYAMA³, Mareki HONMA^{3,4,5}, Yuuki ADACHI³, Ross A. BURNS¹, James O. CHIBUEZE^{6,7}, Yoon Kyung CHOI⁸, Kazuya HACHISUKA³, Kazuhiro HADA^{3,4}, Yoshiaki HAGIWARA⁹, Shota HAMADA¹⁰, Toshihiro HANDA^{10,11}, Mao HASHIMOTO¹², Ken HIRANO³, Yushi HIRATA¹⁰, Takanori ICHIKAWA¹⁰, Hiroshi IMAI^{10,11,13}, Daichi INENAGA¹², Toshio ISHIKAWA³, Takaaki JIKE^{3,4}, Osamu KAMEYA^{3,4}, Daichi KASEDA¹⁰, Jeong Sook KIM¹⁴, Jungha KIM², Mi Kyoung KIM³, Hideyuki KOBAYASHI^{1,2}, Yusuke KONO^{1,2}, Tomoharu KURAYAMA¹⁵, Masako MATSUNO¹⁰, Atsushi MORITA¹⁰, Kazuhito MOTOGI¹⁶, Takeru MURASE¹⁰, Akiharu NAKAGAWA^{10,11}, Hiroyuki NAKANISHI^{10,11}, Kotaro NIINUMA¹⁶, Junya NISHI¹², Chung Sik OH¹⁴, Toshihiro OMODAKA¹⁰, Miyako OYADOMARI¹³, Tomoaki OYAMA³, Daisuke SAKAI³, Nobuyuki SAKAI¹⁴, Satoko SAWADA-SATOH¹⁶, Katsunori M. SHIBATA^{1,2}, Makoto SHIZUGAMI^{3,17}, Jumpei SUDO¹⁰, Koichiro SUGIYAMA¹⁸, Kazuyoshi SUNADA^{3,4}, Syunsaku SUZUKI¹, Ken TAKAHASHI³, Yoshiaki TAMURA^{3,4}, Fumie TAZAKI³, Yuji UENO³, Yuri UNO¹⁰, Riku URAGO¹⁰, Koji WADA¹⁰, Yuan Wei WU¹⁹, Kazuyoshi YAMASHITA³, Yuto YAMASHITA¹⁰, Aya YAMAUCHI³ and Akito YUDA¹⁰

¹Mizusawa VLBI Observatory, National Astronomical Observatory of Japan, Osawa 2-21-1, Mitaka-shi, Tokyo 181-8588

²Department of Astronomical Sciences, SOKENDAI (The Graduate University for Advanced Studies), Osawa 2-21-1, Mitaka-shi, Tokyo 181-8588

³Mizusawa VLBI Observatory, National Astronomical Observatory of Japan, Hoshigaoka 2-12, Mizusawa, Oshu-shi, Iwate 023-0861

⁴Department of Astronomical Sciences, SOKENDAI (The Graduate University for Advanced

Studies), Hoshigaoka 2-12, Mizusawa, Oshu-shi, Iwate 023-0861

⁵Department of Astronomy, Graduate School of Science, The University of Tokyo, Hongo 7-3-1, Bunkyo-ku, Tokyo 113-0033

⁶Centre for Space Research, Physics Department, North-West University, Potchefstroom 2520, South Africa

⁷Department of Physics and Astronomy, Faculty of Physical Sciences, University of Nigeria, Carver Building, 1 University Road, Nsukka, Nigeria

⁸Max-Planck-Institut für Radioastronomie, Auf dem Hügel 69, D-53121-Bonn, Germany

⁹Toyo University, Hakusan 5-28-20, Bunkyo-ku, Tokyo 112-8606

¹⁰Graduate School of Science and Engineering, Kagoshima University, Korimoto 1-21-35, Kagoshima-shi, Kagoshima 890-0065

¹¹Amanogawa Galaxy Astronomy Research Center, Graduate School of Science and Engineering, Kagoshima University, 1-21-35 Korimoto, Kagoshima 890-0065

¹²Faculty of Science, Kagoshima University, Korimoto 1-21-35, Kagoshima-shi, Kagoshima 890-0065

¹³Center for General Education, Institute for Comprehensive Education, Kagoshima University, 1-21-30 Korimoto, Kagoshima 890-0065

¹⁴Korea Astronomy and Space Science Institute, Hwaam-dong 61-1, Yuseong-gu, Daejeon, 305-348, Republic of Korea

¹⁵Teikyo University of Science, 2-2-1 Senju-Sakuragi, Adachi-ku, Tokyo 120-0045

¹⁶Graduate School of Sciences and Technology for Innovation, Yamaguchi University, Yoshida 1677-1, Yamaguchi, Yamaguchi 753-8512

¹⁷NAOJ ALMA Project, National Astronomical Observatory of Japan, Osawa 2-21-1, Mitaka-shi, Tokyo 181-8588

¹⁸National Astronomical Research Institute of Thailand, 260 Moo 4, T. Donkaew, Amphur Maerim, Chiang Mai, 50180, Thailand

¹⁹National Time Service Center, Key Laboratory of Precise Positioning and Timing Technology, Chinese Academy of Sciences, Xi'an 710600, People's Republic of China

*E-mail: tomoya.hirota@nao.ac.jp

Received 2020 January 24; Accepted 2020 February 7

Abstract

We present the first astrometry catalog from the Japanese VLBI (very long baseline interferometer) project VERA (VLBI Exploration of Radio Astrometry). We have compiled all the astrom-

etry results from VERA, providing accurate trigonometric annual parallax and proper motion measurements. In total, 99 maser sources are listed in the VERA catalog. Among them, 21 maser sources are newly reported while the rest of 78 sources are referred to previously published results or those in preparation for forthcoming papers. The accuracy in the VERA astrometry are revisited and compared with those from the other VLBI astrometry projects such as BeSSeL (The Bar and Spiral Structure Legacy) Survey and GOBELINS (the Gould's Belt Distances Survey) with the VLBA (Very Long Baseline Array). We have confirmed that most of the astrometry results are consistent with each other, and the largest error sources are due to source structure of the maser features and their rapid variation, along with the systematic calibration errors and different analysis methods. Combined with the BeSSeL results, we estimate the up-to-date fundamental Galactic parameter of $R_0 = 7.92 \pm 0.16_{\text{stat.}} \pm 0.3_{\text{sys.}}$ kpc and $\Omega_{\odot} = 30.17 \pm 0.27_{\text{stat.}} \pm 0.3_{\text{sys.}}$ km s⁻¹ kpc⁻¹, where R_0 and Ω_{\odot} are the distance from the Sun to the Galactic center and the Sun's angular velocity of the Galactic circular rotation, respectively.

Key words: Astrometry — Galaxy: fundamental parameters — masers

1 Introduction

A distance toward astronomical object is the most fundamental parameter in astronomy and astrophysics. All the physical and dynamical properties of the target sources are estimated based on their distances. The most accurate and reliable method for distance determination is the trigonometric annual parallax measurements. For this purpose, the Hipparcos (Kovalevsky 1998) and the very recent GAIA data release 2 (DR2) (Gaia Collaboration et al. 2018) have presented optical astrometry database for more than 10^5 and 10^9 parallaxes for visible stars with accuracy of 1 mas and a few $10 \mu\text{as}$, respectively. The large number of optical astrometry data play important roles for understanding not only basic properties of each target source but also statistics of various kind of stellar samples such as Hertzsprung-Russell (HR) Diagram, period-luminosity relation of variable stars, and dynamics of our Milky Way Galaxy. However, it is not very easy to access distant sources in the Galactic disk through observations at optical bands because of the extremely high optical extinction. In particular, it is crucial to determine the source distances toward dust/molecular clouds which are seen in the optical and sometimes

infrared dark clouds.

To overcome the above issues, radio astrometry observations have been developed in the last two decades by utilizing the very long baseline interferometer (VLBI) technique (Reid & Honma 2014). When the VLBI array consists of 1000 km baselines, the synthesized beam size (full-width half-maximum, FWHM) of an order of 1 milli-arcsecond (mas) is achievable, as roughly evaluated by $\theta_{\text{mas}} \sim 2000 \times \lambda_{\text{cm}}/D_{\text{km}}$ where λ_{cm} and D_{km} are the observed wavelengths in centimeter and the maximum baseline length in kilometer, respectively. Furthermore, high signal-to-noise ratios (SNR) allow us to measure more accurate positions of target sources than the beam size with the random (or thermal) error of $\sim \theta_{\text{mas}}/2SNR$ (Reid et al. 1988). Usually, the absolute position error in the VLBI astrometry is dominated by the systematic calibration error expressed as $\sim c\Delta\tau\theta_{\text{SA}}/D$, where c , $\Delta\tau$, and θ_{SA} are the speed of light, residual delay in calibration, and separation angle between the target source and calibrator (Reid & Honma 2014). If careful phase calibration are successfully conducted, the high accuracy of VLBI astrometry yield the trigonometric parallax for the 10 kpc (corresponding to 0.1 mas parallax) sources in the Galaxy (Sanna et al. 2017; Nagayama et al. 2020a).

For this purpose, the VLBI Exploration of Radio Astrometry (VERA) project has been initiated in early 2000 by National Astronomical Observatory of Japan (NAOJ). VERA is designed to dedicate for the VLBI astrometry observations to reveal 3-dimensional velocity and spatial structures in the Galaxy. The observational targets are mostly limited to strong maser sources distributed across the Galaxy, with nearby position (phase) calibrators. The construction was completed in 2002 followed by scientific verification observations to establish method for accurate calibration and astrometry data analysis. Regular operations of VERA observations were started in 2004 and the first astrometry results were published in 2007 (Honma et al. 2007; Hirota et al. 2007). Until the end of 2019, more than 60 papers have been published to report results of VERA astrometry observations of Galactic maser sources associated with young stellar objects (YSOs) and late-type stars mostly in the asymptotic giant branch (AGB) and red supergiant (RSG) stars, as summarized in Table 1.

At almost the same time, the Very Long Baseline Array (VLBA) legacy program named The Bar and Spiral Structure Legacy (BeSSeL) Survey has also been carrying out intensive VLBI astrometry observations mainly for distant Galactic high-mass star-forming regions (SFRs) associated with masers (Reid et al. 2009a). Other VLBI arrays such as the European VLBI Network (EVN) and the Australian Long Baseline Array (LBA) are also conducting VLBI astrometry for maser sources in high-mass SFRs by using the 6.7 GHz CH_3OH masers (Rygl et al. 2010; Krishnan et al. 2015; Krishnan et al. 2017). As for low-mass nearby SFRs, an-

other VLBA legacy survey, Gould’s Belt Distances Survey (GOBELINS), observes non-thermal radio emission from T-Tauri stars to measure their trigonometric annual parallaxes (Loinard et al. 2008; Dzib et al. 2016; Kounkel et al. 2017; Ortiz-León et al. 2017; Ortiz-León et al. 2018a). Along with these surveys, number of VLBI astrometry observations have been applied to various population of stellar radio emissions (Reid & Honma 2014).

The primary aim of this paper is to compile all the published astrometry results from VERA to establish the first VERA catalog (Section 4). We also report some of new astrometry results from VERA in the present paper. The results will be compared with those of the other VLBI astrometry projects, BeSSeL (Section 5.1) and GOBELINS (Section 5.2). Based on the latest VERA astrometry dataset, we will revisit their accuracy and possible error sources of astrometry (Section 5.3). Thus, we mainly concentrate on the maser astrometry data for the samples of YSOs in SFRs and AGBs/RSGs in the present paper. The up-to-date Galactic constants will be estimated using all the available VLBI astrometry data (Section 5.4) based on the similar method discussed previously (Reid et al. 2009b; Honma et al. 2012; Reid et al. 2014b; Honma et al. 2015; Reid et al. 2019).

2 Observations

Although details are described in each paper, here we summarize general information about VERA astrometry observations. VERA is consisted of four 20 m radio telescopes in Japan; at Mizusawa, Iriki, Ogasawara, and Ishigaki-jima stations. The baseline lengths of VERA ranging from 1020 to 2270 km provide the synthesized beam size of 1.2 mas and 0.7 mas at 22 GHz and 43 GHz, respectively. We have mainly carried out astrometry observations using the $6_{1,6}-5_{2,3}$ transition of H_2O at 22.235080 GHz (Pickett et al. 1998). Some of the observations have been conducted for the $J=1-0$ SiO maser transitions at 43.122075 GHz and 42.820586 GHz for $v=1$ or/and $v=2$, respectively (Müller et al. 2001). To measure trigonometric annual parallaxes of maser sources, we usually carry out monitoring observations at least for 1 year and sometimes 2 years or longer. In some cases, monitoring observations are interrupted due to shorter life time of the target masers. A typical interval of monitoring is 1-2 months depending on the variability of masers; more variable sources such as AGB stars and low-mass YSOs are observed in shorter interval than 1 month. To achieve better UV coverage, each epoch of observation lasts from horizon to horizon for about 5-10 hours depending on the source declination (i.e. maximum elevation). In a single horizon-horizon track, we observe one or two maser sources. In case of observations of two different sources, we switch the target sources every 10 minutes.

VERA astrometry observations are carried out with the dual-beam receiving system (Honma et al. 2008a). A pair of target maser source and reference continuum source (calibrator) is observed with two receivers simultaneously. The separation angle of these two sources is limited to 0.3-2.2 degrees. Reference sources are mainly selected from the VLBA Calibrator Catalog (Beasley et al. 2002), for which absolute positions are determined with \sim sub-mas accuracy. Some of the calibrators have been newly detected by using fringe-check survey observations with VERA at 22 GHz and/or 43 GHz (Petrov et al. 2007; Petrov et al. 2012). In addition to reference sources, bandpass and delay calibrator(s) are observed every 60-80 minutes. Amplitude calibrations are done through the chopper-wheel method (Ulich & Haas 1976). Typical system noise temperatures are 100 K and 200 K at 22 GHz and 43 GHz, respectively, under good weather condition. However, they become higher by a factor of 2 or larger (>200 K at 22 GHz and >400 K at 43 GHz) under the conditions of high humidity and temperature, in particular at the southern isolated islands, Ogasawara and Ishigaki stations, and/or in the summer season.

VERA can configure various frequency settings and recording settings, such as spectral resolution, total bandwidths, number of intermediate frequency (IF) channels and spectral channels within each IF. Details of the set-up in each observation can be seen in the respective original papers. In most of the observations, the digital filter output provides 16 IF channels with 16 MHz bandwidth (Iguchi et al. 2005). Only left-handed circular polarization is received and sampled with 2-bit per second at 1 Gbps. Dual-polarization observation mode is under commissioning at this moment. One of the 16 MHz IF channels is assigned to the target maser source and the rest of 15 IF channels are assigned to the reference source. For masers, a spectral resolution is set to be 15.625 kHz or 31.25 kHz, corresponding to a velocity resolution of 0.21-0.42 km s⁻¹ or 0.11-0.22 km s⁻¹ at 22 GHz and 43 GHz, respectively. Data were recorded with magnetic tapes before 2015 while more recently hard disk recording system is employed. The newly developed system will be capable of wider-band recording up to 16 Gbps (Oyama et al. 2016). Correlation processing were made with the FX hardware correlator located at NAOJ Mitaka campus until early 2015 (Chikada et al. 1991). From 2015, regular operation of newly developed software correlator has been started in NAOJ Mizusawa campus (Oyama et al. 2016). An accumulation period in the correlation process is 1 second to produce visibility data for further post-processing data analysis.

To achieve accurate phase calibration, reference sources are required to have flux densities higher than ~ 50 -100 mJy on average (in case of 1 Gbps recording rate) to detect their fringes with the SNR of at least 5 within a coherence time of 1-2 minutes and the recording bandwidths

of 240 MHz under the best weather condition. Target maser sources are detectable with the peak intensities of $\sim 1 \text{ Jy beam}^{-1}$ after successful phase-referencing analysis.

3 Data analysis

Basic procedures for calibration and synthesis imaging are summarized in the early results from VERA (Honma et al. 2007; Hirota et al. 2007). Calibration processes and its accuracy, in particular possible error sources by atmospheric calibration, station positions, dual-beam calibration, and source structure effects are reported in separate papers (Honma et al. 2008a; Honma et al. 2008b; Honma et al. 2010; Nagayama et al. 2020a). Only overall characteristics of astrometric accuracy will be discussed in the present paper.

Before the calibration, delay tracking models are re-calculated using a software based on the CALC software package developed for the geodetic VLBI observations (Manabe et al. 1991; Jike et al. 2009) because a priori models employed in the correlation processing are inaccurate for astrometry. In the recalculations, phase-tracking center positions of the target maser sources are shifted to the actual position of maser features within $\sim 100 \text{ mas}$. In the subsequent astrometry calibrations, more accurate delay tracking are done by using the following dataset: Tropospheric and ionospheric delays are recalculated based on the GPS measurements and meteorological data (Honma et al. 2008b; Nagayama et al. 2020a), the earth orientation parameters are taken from the International Earth rotation and Reference systems Service (IERS), and the antenna positions are measured through regular monthly geodetic observations with VERA at 22 GHz (Jike et al. 2009; Jike et al. 2018). For the dual-beam observations, path lengths between two receiving systems for masers and reference sources are calibrated by injecting artificial noise source on the dishes (Honma et al. 2008a), which is so-called "horn-on-dish method". Overall calibration errors are estimated to be 10-20 mm for the tropospheric zenith delay, 3-10 TECU for the ionospheric delay, 3 mm for the antenna position, and 0.1 mm for the instrumental optical path lengths between two beams, as summarized in Nagayama et al. (2020a) and references therein.

Other calibration processes are done in a standard manner of VLBI observations using the NRAO Astronomical Image Processing System (AIPS) software package. Amplitude calibrations are done by the AIPS task APCAL and ACCOR, while a template method is employed by using the AIPS task ACFIT in case of problems in chopper-wheel methods. The instrumental delays and phase offsets among all of the IF channels are determined by the AIPS task FRING on strong calibrator sources, and residual phases are also determined by the AIPS

task FRING on reference sources. These delay and phase calibration solutions are copied to the target maser sources by the AIPS task TACOP, and are applied to the target maser sources by the AIPS task CLCAL. If the reference sources are too weak to detect fringes, so-called inverse phase-referencing are carried out in which maser sources are used for phase calibration (Hirota et al. 2011; Imai et al. 2012; Burns et al. 2015). Synthesis imaging and deconvolution were performed using the AIPS task IMAGR.

After making images of target maser sources at all spectral channels in all observing epochs, each maser spot and feature are identified. A maser spot is defined as an emission component of a single velocity channel and a feature is used for a group of spots in consecutive velocity channels at position coincident with each others. The maser spots and features are identified by the Gaussian fitting (AIPS tasks JMFIT or SAD) with certain threshold of noise levels in a single-channel map and integrated intensity images, respectively.

Some of the data are analyzed by using the VEDA (VEra Data Analyzer) package developed by the VERA project for our own astrometry data (Honma et al. 2007; Honma et al. 2011; Niinuma et al. 2011; Chibueze et al. 2014a; Yamauchi et al. 2016). More details of the VEDA package will be presented in the forthcoming paper (Nagayama et al. 2020b).

The identified maser spots or features are used to determine their proper motions and trigonometric annual parallaxes by fitting the positional offsets in right ascension and declination as a function of time. The fitting parameters are the trigonometric annual parallax π , right ascension and declination offset with respect to the tracking center position at the first epoch of observation, $(\Delta\alpha \cos\delta, \Delta\delta)$, proper motions in right ascension and declination, $(\mu_x, \mu_y) \equiv (\mu_\alpha \cos\delta, \mu_\delta)$. If the astrometric accuracy is significantly worse in declination compared with that in right ascension due to different path length error in the atmospheric calibration (Nagayama et al. 2020a), only the latter data are employed to determine the parallax. If there are multiple maser spots or features, position offsets and proper motions for all the spots/features are fitted simultaneously with the common parallax value.

Usually, the post-fit residual of the fitting is much larger than the astrometric accuracy expected from the thermal noise. This can be interpreted that there could be systematic calibration errors in the fitting results. Thus, the errors of these best-fit parameters are estimated by adding the noise floor to all the astrometry results in order to set the reduced χ^2 value of unity (Honma et al. 2007; Reid et al. 2009a) This additional noise floor is regarded as the total error of astrometry including both systematic and random (thermal) errors.

In case of VERA, error estimation is different from paper to paper. If there are multiple masers, two different approaches have been employed: One is to derive proper motions for

individual features and common parallax for all features simultaneously by the least squares fitting. In this case, the fitting error is regarded as the parallax uncertainty. Another method is to derive parallax value for each maser feature and average all these values. In this case, the standard deviation of these parallaxes is regarded as an uncertainty. However, if the error source of astrometry is dominated by the calibration error of atmospheric phase fluctuation, they are common for all the features and hence, averaged parallax (the latter case) would include systematic errors which are common for all parallax values. Thus, the formal uncertainty could underestimate the error in the averaged parallax value. Although astrometry analysis methods are different from source to source in Table 1, future update of the VERA catalogue will be done by using the unified methods through the new data analysis software package VEDA (Nagayama et al. 2020b).

4 Results

In Table 1, we compile all the parallax measurements that have been conducted with VERA to date. In total, 99 of maser sources are listed. We include some sources in Table 1 for which only parallax values are reported (i.e. no proper motion data). New astrometry results from VERA are reported for 21 sources for the first time in the present paper, while the others have been or will be published last column of Table 1. Most of the target sources are observed with the 22 GHz H₂O masers, and 2 sources, Orion KL (Kim et al. 2008) and R Aqr (Kamohara et al. 2010; Min et al. 2014), are observed in the 43 GHz vibrationally excited SiO masers. Numbers of YSOs in SFRs and late-type stars (AGBs and RSGs) are 68 and 31, respectively. Some of the target sources classified as AGBs include possible candidates of post-AGB stars or young planetary nebulae, such as IRAS 18286–0959 (Imai et al. 2013) and K3-35 (Tafuya et al. 2011). Since the population of RSGs are relatively small, only 2 sources, VY CMa (Choi et al. 2008) and PZ Cas (Kusuno et al. 2013) are reported.

We refer the astrometry data from the original papers as listed in the last column in Table 1. Numbers of significant digits of astrometric parameters are different from source to source, depending on the relative uncertainties. We simply set the uniform number of significant digit for the parameters in Table 1 except for the parallax values, for which we follow the definition of the original papers.

For proper motions, we need additional consideration in some cases. When the target sources are associated with multiple maser features, many literature calculated their averages to estimate systemic motions which are regarded to represent those of central stars. On the other

hand, if there are insufficient number of maser feature(s) in a target source, a proper motion of single feature is used to estimate its systematic motion. If there is no explicit discussion on proper motions in the original paper, we calculate these values as mentioned above. In most of the VERA results, errors in the proper motions are determined by the formal uncertainties in the fitting in case of sources with a single feature or the mean proper motions of multiple maser features. To ensure the use of an accurate estimate of the source systemic proper motion in modelling the Galactic rotation, it is necessary to separate observed proper motions into their respective contributions from the internal proper motions caused by jets, outflows etc., and the true motion of the SFRs in the sky plane. In cases where the proper motions are symmetric or random, this can be done by simply averaging all measured proper motions. However, in asymmetrically sampled cases, or cases of few detected maser features, the average motion may misrepresent the source proper motion. This consequently introduces errors into the evaluation of the model parameters during fitting. We did not consider such potential systematic uncertainties in the proper motions in Table 1. However, if a large enough sample of sources is used then these errors introduced should average out.

The radial velocities of the target sources, which are usually measured by the radio molecular lines such as CO and NH₃ or by the maser lines themselves, are also listed in Table 1. Similarly, these radial velocities could result in significant amount of uncertainties in the estimated 3-dimensional velocity field of the Galaxy. In particular, the definition of the radial velocities would affect the estimation of the systemic velocity of the target sources depending on either average or central velocities of the maser features. It is known that the H₂O masers show sometimes extremely high velocity features up to 10-100 km s⁻¹ with respect to the systemic velocity (Motogi et al. 2016). For instance, one of the target sources, IRAS 20255+4032, shows the average velocity of the four maser features of -63.3 km s⁻¹, while the systemic velocity is determined by the CO line to be -18.2 km s⁻¹ (Sakai et al. 2020c). In such cases, maser data will lead erroneous assumption of the systemic velocities. If there is no estimation of uncertainties in the radial velocity, we take into account these uncertainties of 5 km s⁻¹ as indicated in Table 1. Although the BeSSeL project employs the more conservative value of 10 km s⁻¹, our results are not severely affected these different assumptions.

5 Discussion

In this section, we will revisit discussion on accuracy of the VERA astrometry and estimation of the Galactic fundamental parameters, as reported in previous summary papers (Reid et al.

2009b; Honma et al. 2012; Reid & Honma 2014; Reid et al. 2014b; Honma et al. 2015; Reid et al. 2019).

5.1 Comparison with VERA and VLBA/EVN results

Figure 1 compares the results of parallax measurements carried out by VERA and VLBA/EVN. For this plot, most of the target sources are the H₂O and/or CH₃OH maser sources which are identified in the same SFRs within 1' as listed in Table 2. Some of high-mass SFRs host multiple YSOs associated with different maser clusters within individual regions. We do not include such sources because they could be located in different molecular clouds aligned along the line-of-sight by chance. Only exceptions are Orion KL and HH 12-15 which are observed in radio continuum emission (Menten et al. 2007; Dzib et al. 2016). For Orion KL, we refer to Menten et al. (2007), although there are multiple/different VLBI astrometry results for different YSOs in the same region (see more discussion in the next section). To compare these VLBI astrometry results with each other, we employ the astrometric parameters from VLBA/EVN reported in original references with the highest accuracy data for each source rather than those compiled in Reid et al. (2019) because some of their results are averaged value of multiple VLBI astrometry results. For G359.62–00.25 and Sgr D/G001.14–00.12, we use the parallax values in Reid et al. (2019) because the references are in preparation.

As seen in the clear correlation in Figure 1, most of the astrometry results are consistent within a factor of 1.5 except for a few sources with larger scatter. They are IRAS 05137+3919/G168.06+00.82 (Honma et al. 2011; Hachisuka et al. 2015), Sgr D/G001.14–00.12 (Sakai et al. 2017; Reid et al. 2019)¹, G005.88–00.39 (Motogi et al. 2011; Sato et al. 2014), and G048.60+00.02 (Nagayama et al. 2011a; Zhang et al. 2013). These data show differences larger than a factor of 2.

To compare their differences, we calculate the normalized parallax differences scaled by their joint uncertainties, as defined by the following equation;

$$\Delta\pi/\sigma_{\Delta\pi} \equiv \frac{\pi_{\text{VERA}} - \pi_{\text{VLBA}}}{\sqrt{\sigma_{\text{VERA}}^2 + \sigma_{\text{VLBA}}^2}} \quad (1)$$

in which π_{VERA} and π_{VLBA} are the parallaxes measured with VERA and VLBA, respectively, and σ_{VERA} and σ_{VLBA} are the parallax errors for VERA and VLBA results, respectively. The results are listed in Table 2 and the distribution is plotted in Figure 2. As seen in Figure 2, most of the target sources give consistent results within $\Delta\pi/\sigma_{\Delta\pi} < 3$ or less than 3σ limit.

¹ Although it is the largest error bar in the plot, we could not confirm the original reference in Reid et al. (2019).

The first quartile, median, and third quartile are -0.65 , 0.35 , and 1.49 , respectively. The largest discrepant measurements are for G048.60+00.02 (12.32), G005.88–00.39 (8.28), S269 (-3.61), G135.28+02.80 (-3.43), and IRAS 05137+3919 (-3.18). Sgr D/G001.14–00.12 give the smaller value of 1.26 due to the exceptionally large relative errors of VLBA parallax of $\sim 80\%$. We note that the possible systematic errors in the VERA parallax as discussed in the last paragraph of Section 4 are not included in the calculated $\Delta\pi/\sigma_{\Delta\pi}$. Thus, parallax measurements from VERA and VLBA/EVN for 23 out of total 28 samples (82%) agree with each others within 3σ levels.

Possible origins of such large errors are due to insufficient number of observing epochs, in particular around the peak season of the annual parallax value (for IRAS 05137+3919), or errors in the atmospheric calibration and VERA dual-beam phase calibrations (for G048.60+00.02). These results could be improved by using additional data and re-calibration processing. Furthermore, spatially extended structures of the target maser features could significantly degrade the accuracy of the position measurements of the maser features, which would introduce additional errors in the astrometry and hence, derived parallax values. In fact, the possible effect of such maser structures is intensively discussed for a high-mass YSO S269 at the distance of 4 kpc (Honma et al. 2007; Asaki et al. 2014; Quiroga-Nuñez et al. 2019), in which the possible structure effect results in a parallax error of $>20\%$. It has been already discussed for the VERA data (Honma et al. 2010) and we will revisit this issue in the next sections.

5.2 Comparison for distances toward nearby SFRs

Several astrometry results are reported for the Orion Molecular Cloud both with VERA and VLBA since the beginning of the VERA and VLBA astrometry projects (Hirota et al. 2007; Kim et al. 2008; Sandstrom et al. 2007; Menten et al. 2007; Kounkel et al. 2017) including the new result from VERA (Nagayama et al. 2020b). In the central part of the Orion region, active high-mass SFRs Orion KL and Orion Nebular Cluster (ONC) are of great interest. The VERA results are for observations of the H_2O masers or SiO masers (Orion Source I), while VLBA observes radio continuum emission from different non-thermal radio emitting YSOs in the ONC region. The first astrometry results for these sources had larger uncertainties of 437 ± 19 pc (Hirota et al. 2007) and 389^{+24}_{-21} pc (Sandstrom et al. 2007) from the VERA H_2O maser and VLBA 15 GHz continuum observations, respectively. Subsequent higher accuracy data of 418 ± 6 pc from the SiO masers with VERA (Kim et al. 2008) and 414 ± 7 pc from the 8 GHz continuum with VLBA (Menten et al. 2007) are in excellent agreement. These results suggest a

weighted-mean distance of 416.3 ± 4.6 pc toward the Orion KL region or the central part of the ONC. On the other hand, recent comprehensive studies with VLBA by Kounkel et al. (2017) suggest a smaller distances of 388 ± 5 pc as a weighted average of distances of YSOs in wider area of ONC.

The possible reason for the differences in these parallax measurements, in particular compared with that of Menten et al. (2007), are discussed in Kounkel et al. (2017), which are attributed to the different number of samples, systematic errors originated from ionospheric calibration, multiplicity of the target sources, and/or different treatment of the data for the fitting (e.g. fitting routine for the right ascension and/or declination). If this difference is real, it would suggest the depth of the region along the line-of-sight; Source I could be located in the rear side of the ONC which argues against Kim et al. (2008).

For other nearby low-mass star-forming regions, we have carried out series of astrometry observations (Imai et al. 2007; Hirota et al. 2007; Hirota et al. 2008a; Hirota et al. 2008b; Kim et al. 2008; Hirota et al. 2011). Similar comprehensive survey are also carried out by the VLBA large program GOBELINS and their pilot surveys (Loinard et al. 2008; Dzib et al. 2016; Kounkel et al. 2017; Ortiz-León et al. 2017; Ortiz-León et al. 2018a). Some of the target regions are common, such as Orion, Monoceros, Ophiuchus, and Perseus molecular clouds. In Figure 1, only Orion KL, HH 12-15, and IRAS 16293–2422 in L1689 are plotted as they are regarded as the same SFRs observed with VERA.

We quantitatively compare the difference in distances between two astrometry measurements. Here we compare distances rather than parallaxes because many literature listed mean distances of multiple sources. In the following discussion, the error in the distance difference is calculated from the root sum square of each distance error, and the error in each distance is estimated from the geometric mean of both error bars (i.e. $\Delta D = \sqrt{D_1 D_2}$ in case of $D_{-D_2}^{+D_1}$). The difference between relative errors in the parallax and distance estimated above are as small $< 0.1-0.3\%$.

For the Orion regions, GOBELINS also includes various molecular clouds outside Orion KL. One of examples is the L1641 region at the measured distance of 428 ± 10 pc (Kounkel et al. 2017). The VERA result for another nearby maser source, L1641 S3, presents the slightly larger distance of 473_{-27}^{+32} pc. The difference in these two distance values of 45 ± 31 pc is not significant with the only 1.5σ level. Although VLBA failed to determine the parallax of YSOs in λ Ori possibly due to scattering at the lower frequency (Kounkel et al. 2017), we can measure the parallax of a YSO associated with the λ Ori region, B35, to be 1.98 ± 0.25 mas in the present paper, corresponding to the distance of 505_{-57}^{+73} pc. The difference in distances between

those from GAIA DR2, $402 \pm 1 \pm 20$ pc (Zucker et al. 2019), and VERA is 103 ± 68 pc, which is 1.5σ level. Because the uncertainty in the parallax value from VERA is still large, future more accurate observations are required to confirm the result.

For YSOs in the Monoceros region, HH (or GGD) 12-15, distances from VERA and VLBA of 620_{-110}^{+180} pc (present paper) and 893_{-40}^{+44} pc (Dzib et al. 2016), respectively, are different by a factor of 45%. The difference in these two distances is -273 ± 147 pc. The error bar of the VERA result, $\sim 20\%$, is relatively larger than the typical value (see Figure 3) as discussed in the next section.

For the Ophiuchus region, the distances measured by GOBELINS are 137.3 ± 1.2 pc and 147.3 ± 3.4 pc toward dark clouds L1688 and L1689, respectively (Ortiz-León et al. 2017). Parallax measurements for a protostar IRAS 16293–2422, which is located in L1689, give 178_{-37}^{+18} pc and 141_{-21}^{+30} pc from VERA (Imai et al. 2007) and VLBA (Dzib et al. 2018), respectively. These two values from maser astrometry marginally agree with each other (37 ± 36 pc), but the smaller distance of ~ 140 pc is more consistent with those from continuum sources in L1689.

Comparing with the GAIA DR2 results, VLBA results are confirmed to be in good agreement for Ophiuchus (Ortiz-León et al. 2017; Ortiz-León et al. 2018b) and Perseus (Ortiz-León et al. 2018a) regions. In case of another nearby SFR, NGC2264, the distance measured with VERA of 738_{-50}^{+57} pc (Kamezaki et al. 2014a) is in good agreement with the GAIA DR2 value, 719 ± 16 pc (Maíz Apellániz 2019). The mean distance toward slightly farther molecular clouds in Gem OB1, IRAS 06058+2138 (Oh et al. 2010), IRAS 06061+2151 (Niinuma et al. 2011), and S255 IR-SMA1 (Burns et al. 2016), of 1.85 kpc (with a standard deviation of 0.14 kpc) is also consistent with that from the GAIA DR2 result, $1.786 \pm 0.004 \pm 0.089$ kpc (Zucker et al. 2019). On the other hand, some of the parallax values derived from VERA observations showed significantly large uncertainties which are larger than the error bars of VLBA and GAIA results. In the case of Perseus Molecular Cloud, the VERA results of 234 ± 13 pc from the weighted mean distance of NGC 1333 (Hirota et al. 2008a) and L1448 (Hirota et al. 2011) is smaller by -59 ± 26 pc than that of GAIA DR2 of 293 ± 22 pc (Ortiz-León et al. 2018a), although the parallax of NGC 1333 was not determined with VLBA alone.

We note that the parallax values of GAIA DR2 would include the zero-point offset with an order of -0.1 – 0 mas (Gaia Collaboration et al. 2018). More detailed analysis are presented in Xu et al. (2019) and references therein, suggesting that the parallax offset in the GAIA DR2 data is -75 ± 29 μ as. It requires the correction of the parallax value corresponding to the systematic uncertainty from -1.5 pc to -180 pc at the distance of 140–1800 pc in the

SFRs discussed above. This effect is already considered as the possible systematic error in each reference. In addition, the parallax offset in the GAIA DR2 data would affect more significant in the farther target sources. Thus, the large differences in the parallax values for nearby SFRs are mostly due to shorter lifetime of the H₂O masers associated with the low-mass YSOs than the period of annual parallax (i.e. 1 year), and there seems no significant contribution from the zero-point offset in the GAIA DR2 parallaxes. In addition, significant spatial structures of the nearby sources could degrade the accuracy of the position measurements (Imai et al. 2007; Hirota et al. 2008b; Honma et al. 2010; Dzib et al. 2018). We will evaluate this effect in the next section.

5.3 Accuracy and dominant error sources in VERA Astrometry

As discussed in Honma et al. (2010), a motion of 0.5 km s⁻¹, which is comparable to typical line widths of the masers (full-width half-maximum of 1 km s⁻¹), corresponds to the transverse distance of 0.1 au within 1 yr. If the motion is systematic, it can partly contribute to the linear proper motion and hence, is measurable by the VLBI astrometry monitoring. However, if such a motion is originated from a turbulence in the maser cloud, it could cause change in the structure of the maser feature randomly. The possible structure change would affect the positional accuracy of the maser features. As a result, this effect will lead to the error in the annual parallax, which is equal to the angular size of 1 au at the distance of the target source, up to 10%. Even larger errors up to 20% or corresponding structure changes of 0.2 au scale would be likely, given the spatially extended nature of maser features (>1 au).

Figure 3 shows the errors in the parallax as a function of the parallax values. Obviously, the plot shows a clear trend of correlation as seen in the smaller number of samples (Honma et al. 2010). In other word, the errors in the parallaxes are mostly 2-20% independent of the source distances. It is unlikely that the correlation is mostly due to the calibration errors as they should strongly depend on the separation angles between the calibrators and targets, weather condition, and source elevation (declination), rather than their distances.

It should be noted that the larger variation in Figure 3 than that of Honma et al. (2010) would also reflect different calibration errors and/or method of analysis such as different number of maser features employed in the parallax fitting and lengths of astrometry monitoring observations. In general, lower declination sources at $\delta < -30$ degrees, such as NGC6334(I), are more seriously affected by atmospheric calibration errors (Chibueze et al. 2014a). However, we confirm that the correlation of parallaxes and their errors would be the results of source

structures.

For the AGB stars, trigonometric parallax measurements can be done by using the VLBI astrometry of maser sources and optical astrometry like Hipparcos and GAIA (DR2). One example for a semi-regular variable star SV Peg demonstrates that there could be significant differences between VLBI and GAIA DR2 astrometry, for which parallax values are 3.00 ± 0.06 mas and 1.12 ± 0.28 mas, respectively (Sudou et al. 2019). The discrepancy is most likely attributed to an effect of unresolved structure of the stellar photosphere observed with GAIA DR2. Xu et al. (2019) discussed accuracy of parallax measurements of YSOs, AGBs, and pulsars from VLBI astrometry and GAIA DR2, and found the largest differences in the AGB samples. More detailed comparison of astrometry observations for each AGB star will be discussed in a separate paper (Matsuno et al. 2020; Nakagawa et al. 2020) and hence, it is out of the scope of this paper.

The structure effect is though to be more serious for highly variable sources such as low-mass nearby YSOs and AGB stars (Imai et al. 2007; Hirota et al. 2008b). In contrast, it is demonstrated that astrometry for the compact stellar emission could achieve $<1\%$ parallax accuracy for nearby open cluster Pleiades (Melis, et al. 2014) and continuum sources in the nearby Ophiuchus molecular clouds (Ortiz-León et al. 2017). The structure changes in maser features are found to be less significant for farther (~ 10 kpc) sources because the other error budgets, in particular due to calibration errors of tropospheric delay term (Honma et al. 2008b; Nagayama et al. 2020a), become more significant than those from the source structure. Hence, we note that target maser sources should be selected carefully according to their spatial structures in the synthesized images to overcome this issue. It is also important to make images with better uv coverages to recover both spatially compact and extended emission components. In case of VERA, lack of shorter baselines (<1000 km) would seriously resolve out spatially extended maser features. Thus, further KaVA (KVN and VERA Array) and EAVN (East Asian VLBI Network; An et al. 2018) are expected to improve the accuracy of the maser astrometry.

5.4 Galactic Structure

The currently available VLBI astrometry results are plotted in Figure 4. We plot positions of SFRs and RSGs but AGBs are not included because these sources will not be used for the further analysis as discussion later. Thus, total 224 sources are selected including both VERA and other VLBI results (Reid et al. 2019). We indicate the location of the best-fitted Galactic spiral arms determined by Reid et al. (2019). Most of the target sources are located in the

northern hemisphere with the declination of $\delta > -35$ degrees because of the visibility of the target sources from VERA, VLBA, and EVN. Thus, the sample distribution is strongly biased to the first and second Galactic quadrants ($0 \text{ deg} < l < 180 \text{ deg}$, where l is the Galactic longitude), while less number of sources are located in the third quadrant ($180 \text{ deg} < l < 270 \text{ deg}$). Only exceptions are two sources, G339.884–1.259 (Krishnan et al. 2015) and G305.2 region (Krishnan et al. 2017), which are observed with the Australian LBA, as plotted in the fourth quadrant ($270 \text{ deg} < l < 360 \text{ deg}$) of Figure 4. The most distant parallax measurement with VLBI is achieved for a high-mass SFR G007.47+00.05 with the trigonometric parallax from the BeSSeL project of 0.049 ± 0.006 mas, corresponding to $20.4_{-2.2}^{+2.8}$ kpc (Sanna et al. 2017). This value is consistent with the astrometry observations with VERA of 20 ± 2 kpc, which is estimated based on the absolute proper motions and radial velocity measurements and 3-dimensional Galactic rotation model (Yamauchi et al. 2016).

The Galactic rotation can be seen in Figure 5 in which positions of maser sources are plotted with 2-dimensional velocity vectors in the Galactic plane. The 2-dimensional vectors in the Galactic plane projection are determined by combination of sky plane and line of sight velocities as mentioned in Section 4. To transform from the measurements in a Heliocentric frame to the Galacto-centric reference frame, we employ the Galaxy model with the power-law rotation curve as discussed below. The parameters used for the transformation are summarized in Table 3. We also assume the Solar motion of $(U_{\odot}, V_{\odot}, W_{\odot}) = (11.1, 12.24, 7.25)$ in km s^{-1} (Schönrich et al. 2010). The Galactic rotation curve can be constructed as plotted in Figure 6 using the same parameter set. The well known flat rotation curve is confirmed toward the distance up to 15 kpc from the Galactic center.

By combining currently available maser astrometry results from VERA, VLBA, EVN, and LBA, we can estimate the fundamental parameters of the Milky Way Galaxy as discussed in Honma et al. (2012) by using increased number of samples. Here we briefly summarize our data analysis. We employ SFRs and high-mass RSGs but exclude AGB stars for our data analysis. This is because dynamical properties of AGB stars are different from those of former samples, such as velocity dispersion and peculiar motions with respect to the Galactic rotation (known as asymmetric drift). In the model fitting, outliers which have the Galacto-centric distances within < 4 kpc or the peculiar motion of $V > 50 \text{ km s}^{-1}$ are also removed from the input data for further analysis to avoid systematic errors in the estimated parameters. The former condition is considered to exclude systematic motion caused by the Galactic bar (Honma et al. 2012; Reid et al. 2014b). These sources are indicated by gray symbols in Figures 5 and 6. The number of removed sources is 35, and hence, we used total 189 sources for the further analysis, which are

plotted by blue symbols in Figures 5 and 6.

In the Galaxy model, we simply assume the circular rotation of the Local Standard of Rest (LSR) with small systematic/random motions. The distances toward the Galactic center and the rotation velocity of the LSR around the Galactic center are referred to R_0 and Θ_0 , respectively. The ratio of Θ_0/R_0 gives the Galactic angular velocity at the LSR, Ω_0 . As discussed previously, we will solve a set of R_0 and Ω_0 , rather than R_0 and Θ_0 because the latter set is known to be tightly correlated (Reid et al. 2009b; Honma et al. 2012). Although the correlation could become modest due to increased number of target sources in larger distribution of our present data, we follow the same data analysis by Honma et al. (2012) to compare the results consistently. For the Galactic rotation curve, we use two different models; a power law, $\Theta(R) = \Theta_0(R/R_0)^\alpha$, and 2nd-order polynomial, $\Theta(R) = \Theta_0 + a_0(R - R_0) + b_0(R - R_0)^2$, functions of rotation curves. The power-law index α , or the polynomial coefficients a_0 and b_0 are also solved in the analysis. In addition, mean systematic motions, (U_s, V_s, W_s) are introduced in the models to account for the peculiar motions (Reid et al. 2009b; Honma et al. 2012). The U_s , V_s , and W_s are defined as the velocity components toward the Galaxy center, the direction of Galactic rotation, and the north Galactic pole, respectively. The Solar motion is assumed to be $(U_\odot, V_\odot, W_\odot) = (11.1, 12.24, 7.25)$ in km s^{-1} (Schönrich et al. 2010).

All the parameters are estimated by the same procedures described in Honma et al. (2012), based on the Markov Chain Monte Carlo (MCMC) method. To explore the posterior probability distribution of the parameters, MCMC simulation is iterated for the trial number of 10^6 . Figure 7 shows the posterior probability distribution for six parameters of power-law model. For all parameters, the posterior probability distribution shows a single-peaked symmetric structure, which confirms reasonable estimates of the parameters. Table 3 summarize the best parameters and their statistical errors calculated from the means and the standard deviations of the posterior probability distributions in our two Galactic rotation models. As for R_0 and Ω_0 , both results agree well with each other with differences less than 1%. These differences are much smaller than the error bars. The inward motion of U_s is non-zero values in contrast to the previous paper (Honma et al. 2012), while the vertical component with respect to the Galactic plane, W_s suggests no significant motion. The power-law index α of -0.016 ± 0.012 is slightly negative but is consistent with the flat rotation curve.

As listed in Table 3, we can directly compare the present results with the models of ID 14 for the power-law rotation curve and ID 22 for the polynomial rotation curve (removing outliers and adopting fixed $V_\odot = 12 \text{ km s}^{-1}$) in Honma et al. (2012). Present results are in good agreement with those in Honma et al. (2012) but the statistical errors for R_0 and Ω_0 estimated

by the MCMC method are smaller by a factor of ~ 2.5 as the number of samples increases from 49 to 189. In particular, an increase in the number of further sources would significantly contribute to improve the precision.

As reported in the previous paper (Honma et al. 2012), Ω_0 and V_\odot is tightly correlated and Ω_0 is dependent on the adopted value of V_\odot . However, the angular velocity of the Sun defined by $\Omega_\odot \equiv \Omega_0 + V_\odot/R_0$ can be well determined. It is estimated to be $\Omega_\odot = 30.17 \pm 0.27 \text{ km s}^{-1} \text{ kpc}^{-1}$ using R_0 and Ω_0 in the power-law model shown in Table 3 and the adopted value of $V_\odot = 12.24 \text{ km s}^{-1}$ (Schönrich et al. 2010).

As demonstrated in Honma et al. (2012), estimated Galactic fundamental parameters depend on the employed model of the Galaxy and input source samples. In the present paper, we did not perform the MCMC fitting by changing the Solar motion. The assumed values of the Solar motion would lead to systematic errors in the derived parameters and hence, the uncertainties in the estimated parameters could be underestimated. For instance, the difference in R_0 is as small as $< 1\%$ while that of Ω_0 is about 6% when V_\odot is assumed to be 5.25 km s^{-1} or 12.0 km s^{-1} , or is solved in the MCMC analysis to be $\sim 19 \text{ km s}^{-1}$ (Table 5 and Figure 4 in Honma et al. 2012). The different values of the Solar motion also result in the systematic error of Θ_0 of the same magnitude, 6% (Table 6 in Honma et al. 2012). However, it does not strongly affect the Ω_\odot value, which is 0.3% difference (Table 6 in Honma et al. 2012). In summary, assuming the Solar motions in the MCMC analysis would lead systematic errors of 6% in Ω_0 and Θ_0 , while the effect is less than 1% for R_0 and Ω_\odot . In order to take into account the above systematic errors, we estimate the systematic error in R_0 of 4% , adding the 1% of the model dependency (Table 3) and 3% of the sample dependency (Honma et al. 2015). For the Ω_\odot , the systematic error is 1% mainly due to the sample dependency (Honma et al. 2015), given the smaller differences among models in Table 3 (Honma et al. 2012; Honma et al. 2015; Reid et al. 2019).

According to Reid et al. (2019), R_0 and Ω_\odot are determined to be $8.15 \pm 0.15 \text{ kpc}$ and $30.32 \pm 0.27 \text{ km s}^{-1} \text{ kpc}^{-1}$, respectively, based on the VLBI astrometry of 147 maser sources, as listed in Table 4 and 5. Our results considered both errors of the statistic and the systematic, $R_0 = 7.92 \pm 0.16_{\text{stat.}} \pm 0.3_{\text{sys.}} \text{ kpc}$ and $\Omega_\odot = 30.17 \pm 0.27_{\text{stat.}} \pm 0.3_{\text{sys.}} \text{ km s}^{-1} \text{ kpc}^{-1}$ are consistent with each other. Small difference in R_0 could be attributed to the employed Galactic rotation curve in the models and/or the different input samples as noted in the previous paragraph (Honma et al. 2012; Honma et al. 2015). As already discussed in previous papers, new VLBI astrometry results are different from those recommended by the International Astronomical Union (IAU), $R_0 = 8.5 \text{ kpc}$ and $\Theta_0 = 220 \text{ km s}^{-1}$ (Kerr, & Lynden-Bell 1986). Our results yield

$\Theta_0 = R_0 \Omega_0 = 227 \text{ km s}^{-1}$. Thus, R_0 and Θ_0 are smaller by 6% and larger by 3%, respectively. The angular velocity of the Sun, Ω_\odot is independently determined by proper motion measurements of a supermassive black hole at the Galactic center, Sgr A* (Reid & Brunthaler 2004; Reid & Brunthaler 2020). As listed in Table 5, all the results of Ω_\odot are in good agreement. Recently, the distance to Sgr A* is accurately determined to be $R_0 = 8.178 \pm 0.013_{\text{stat.}} \pm 0.022_{\text{sys.}}$ kpc (Gravity Collaboration et al. 2019) and $R_0 = 7.946 \pm 0.050_{\text{stat.}} \pm 0.032_{\text{sys.}}$ kpc (Do et al. 2019) by measurements of stellar orbital motions around Sgr A* (Table 4). Our result is consistent with them. This consistency suggests that Sgr A* is truly located at the dynamical center of the Galactic rotation of LSR. When we adopt $R_0 = 8.178$ kpc (Gravity Collaboration et al. 2019), the Galactic rotation velocity is $\sim 3\%$ upwardly revised to 234 km s^{-1} .

6 Summary and future prospects

We have compiled all the astrometry measurements from VERA to construct the first version of the VERA catalogue. In total 99 target sources are listed in the catalogue including 21 new measurements in the present paper. The results are basically consistent with those from other VLBI astrometry project with VLBA (BeSSeL) and EVN while significant differences are also reported for several sources. It is mainly affected by the spatial structures of the target maser features and their time variation, along with the systematic calibration errors. The effects are more significant for the nearby lower-mass YSOs and AGBs.

Using all the available VLBI astrometry data base, we model the Galactic structure to estimate the fundamental parameters such as the distance toward the Galactic center, R_0 , angular velocity of the LSR around the Galactic center, Ω_0 , and the model of the rotation curve. Using these parameters, the angular velocity of the Sun, Ω_\odot , is calculated to compare with the other results. The results, $R_0 = 7.92 \pm 0.16_{\text{stat.}} \pm 0.3_{\text{sys.}}$ kpc and $\Omega_\odot = 30.17 \pm 0.27_{\text{stat.}} \pm 0.3_{\text{sys.}}$ $\text{km s}^{-1} \text{ kpc}^{-1}$ are also consistent with those from VLBA (Reid et al. 2019).

Further astrometry observations with VERA will be able to advance the studies on the Galaxy model by increasing the number of target sources along with reducing systematic errors due to insufficient samples (Honma et al. 2015). New VLBI array such as KaVA/EAVN and those in southern hemisphere, LBA (Krishnan et al. 2015; Krishnan et al. 2017) and future SKA (Square Kilometer Array) in the VLBI mode (Green et al. 2015) will improve astrometry accuracy for spatially extended sources and southern sources, respectively, which are still insufficient for the currently available VERA catalogue. The new data analysis tool, VEDA, will provide systematic astrometry results for future VERA observational data and

reanalysis of previous archive data (Nagayama et al. 2020b).

Acknowledgments

We are grateful to the referee for valuable comments to improve the manuscript. We would like to thank all the staff of Mizusawa VLBI Observatory of NAOJ to operate the VERA array, correlate the VLBI data, and analyze the results by using VEDA. We also thank staff and students of Kagoshima University VERA Group who involved in telescope operation. T. Hirota is financially supported by the MEXT/JSPS KAKENHI Grant Number 17K05398. HI is supported by the MEXT/JSPS KAKENHI (16H02167). J.O.C. acknowledges support by the Italian Ministry of Foreign Affairs and International Cooperation (MAECI Grant Number ZA18GR02) and the South African Department of Science and Technolgy's National Research Foundation (DST-NRF Grant Number 113121) as part of the ISARP RADIOSKY2020 Joint Research Scheme. Data analysis were in part carried out on common use data analysis computer system at the Astronomy Data Center, ADC, of the National Astronomical Observatory of Japan.

References

- An, T., Sohn, B. W., & Imai, H. 2018, *Nature Astronomy*, 2, 118
- Ando, K. et al. 2011, *PASJ*, 63, 45
- Asaki, Y., Imai, H., Sobolev, A. M., Parfenov, S., & Yu. 2014, *ApJ*, 787, 54
- Beasley, A. J., Gordon, D., Peck, A. B., Petrov, L., MacMillan, D. S., Fomalont, E. B., & Ma, C. 2002, *ApJS*, 141, 13
- Burns, R. A. et al. 2017, *MNRAS*, 467, 2367
- Burns, R. A., Handa, T., Nagayama, T., Sunada, K., & Omodaka, T. 2016, *MNRAS*, 460, 283
- Burns, R. A., Imai, H., Handa, T., Omodaka, T., Nakagawa, A., Nagayama, T., & Ueno, Y. 2015, *MNRAS*, 453, 3163
- Burns, R. A., Nagayama, T., Handa, T., Omodaka, T., Nakagawa, A., Nakanishi, H., Hayashi, M., & Shizugami, M. 2014a, *ApJ*, 797, 39
- Burns, R. A. et al. 2014b, *PASJ*, 66, 102
- Chibueze, J. O., Hamabata, H., Nagayama, T., Omodaka, T., Handa, T., Sunada, K., Nakano, M., & Ueno, Y. 2017, *MNRAS*, 466, 4530
- Chibueze, J. O. et al. 2016, *MNRAS*, 460, 1839
- Chibueze, J. O. et al. 2014a, *ApJ*, 784, 114
- Chibueze, J. O. et al. 2014b, *PASJ*, 66, 104
- Chibueze, J. O. et al. 2019, *PASJ*, 71, 92
- Chibueze, J. O. et al. 2020, submitted to *PASJ*
- Chikada, Y., Kawaguchi, N., Inoue, M., Morimoto, M., Kobayashi, H., & Mattori, S. 1991, *Frontiers*

of VLBI, 79

- Choi, Y. K., Hachisuka, K., Reid, M. J., Xu, Y., Brunthaler, A., Menten, K. M., & Dame, T. M. 2014, *ApJ*, 790, 99
- Choi, Y. K. et al. 2008, *PASJ*, 60, 1007
- Do, T. et al. 2019, *Science*, 365, 664
- Dzib, S. A., Ortiz-León, G. N., Loinard, L., Mioduszewski, A. J., Rodríguez, L. F., Torres, R. M., Deller, A. 2016, *ApJ*, 826, 201
- Dzib, S. A. et al. 2018, *A&A*, 614, A20
- Gaia Collaboration et al. 2018, *A&A*, 616, A1
- Gravity Collaboration et al. 2019, *A&A*, 625, L10
- Green, J., Van Langevelde, H. J., Brunthaler, A., Ellingsen, S., Imai, H., Vlemmings, W., Reid, M., & Richards, A. 2015, *Advancing Astrophysics with the Square Kilometre Array (AASKA14)*, 119
- Hachisuka, K., Brunthaler, A., Menten, K. M., Reid, M. J., Hagiwara, Y., & Mochizuki, N. 2009, *ApJ*, 696, 1981
- Hachisuka, K. et al. 2006, *ApJ*, 645, 337
- Hachisuka, K., Choi, Y. K., Reid, M. J., Brunthaler, A., Menten, K. M., Sanna, A., & Dame, T. M. 2015, *ApJ*, 800, 2
- Hirota, T. et al. 2007, *PASJ*, 59, 897
- Hirota, T. et al. 2008a, *PASJ*, 60, 37
- Hirota, T. et al. 2008b, *PASJ*, 60, 961
- Hirota, T., Honma, M., Imai, H., Sunada, K., Ueno, Y., Kobayashi, H., & Kawaguchi, N. 2011, *PASJ*, 63, 1
- Honma, M. et al. 2007, *PASJ*, 59, 889
- Honma, M. et al. 2008a, *PASJ*, 60, 935
- Honma, M. et al. 2012, *PASJ*, 64, 136
- Honma, M., Hirota, T., Kan-Ya, Y., Kawaguchi, N., Kobayashi, H., Kurayama, T., & Sato, K. 2011, *PASJ*, 63, 17
- Honma, M. et al. 2010, *Publications of the National Astronomical Observatory of Japan*, 13, 57
- Honma, M., Nagayama, T., & Sakai, N. 2015, *PASJ*, 67, 70
- Honma, M., Tamura, Y., & Reid, M. J. 2008b, *PASJ*, 60, 951
- Iguchi, S., Kurayama, T., Kawaguchi, N., & Kawakami, K. 2005, *PASJ*, 57, 259
- Imai, H., Kurayama, T., Honma, M., & Miyaji, T. 2013, *PASJ*, 65, 28
- Imai, H. et al. 2007, *PASJ*, 59, 1107
- Imai, H., Sakai, N., Nakanishi, H., Sakanoue, H., Honma, M., & Miyaji, T. 2012, *PASJ*, 64, 142

Imai, H., Tafoya, D., Honma, M., Hirota, T., & Miyaji, T. 2011, PASJ, 63, 81

Iwata, Y., Kato, H., Sakai, D., & Oka, T. 2017, ApJ, 840, 18

Jike, T., Manabe, S., & Tamura, Y. 2009, Journal of the Geodetic Society of Japan, 55, 369

Jike, T., Manabe, S., & Tamura, Y. 2018, Journal of the Geodetic Society of Japan, 63, 193

Kamezaki, T. et al. 2014a, ApJS, 211, 18

Kamezaki, T., Kurayama, T., Nakagawa, A., Handa, T., Omodaka, T., Nagayama, T., Kobayashi, H., & Shizugami, M. 2014b, PASJ, 66, 107

Kamezaki, T. et al. 2016a, PASJ, 68, 71

Kamezaki, T., Nakagawa, A., Omodaka, T., Inoue, K.-i., Chibueze, J. O., Nagayama, T., Ueno, Y., & Matsunaga, N. 2016b, PASJ, 68, 75

Kamezaki, T. et al. 2012, PASJ, 64, 7

Kamohara, R. et al. 2010, A&A, 510, A69

Kerr, F. J., & Lynden-Bell, D. 1986, MNRAS, 221, 1023

Kim, M. K. et al. 2008, PASJ, 60, 991

Kovalevsky, J. 1998, ARA&A, 36, 99

Koide, N. et al. 2019, PASJ, 71, 113

Kounkel, M. et al. 2017, ApJ, 834, 142

Krishnan, V. et al. 2015, ApJ, 805, 129

Krishnan, V., Ellingsen, S. P., Reid, M. J., Bignall, H. E., McCallum, J., Phillips, C. J., Reynolds, C., Stevens, J. 2017, MNRAS, 465, 1095

Kurayama, T., Nakagawa, A., Sawada-Satoh, S., Sato, K., Honma, M., Sunada, K., Hirota, T., & Imai, H. 2011, PASJ, 63, 513

Kusuno, K., Asaki, Y., Imai, H., & Oyama, T. 2013, ApJ, 774, 107

Loinard, L., Torres, R. M., Mioduszewski, A. J., & Rodríguez, L. F. 2008, ApJL, 675, L29

Maíz Apellániz, J. 2019, A&A, 630, A119

Manabe, S., Yokoyama, K., & Sakai, S. 1991, Earth orientation parameters and celestial and terrestrial reference frames of NAOMIZ analysis, IERS Technical Note 8, 61

Matsumoto, N. et al. 2011, PASJ, 63, 1345

Matsuno, M. et al. 2020, submitted to PASJ

Melis C., Reid M. J., Mioduszewski A. J., Stauffer J. R., & Bower G. C. 2014, Science, 345, 1029

Menten, K. M., Reid, M. J., Forbrich, J., & Brunthaler, A. 2007, A&A, 474, 515

Min, C., Matsumoto, N., Kim, M. K., Hirota, T., Shibata, K. M., Cho, S.-H., Shizugami, M., & Honma, M. 2014, PASJ, 66, 38

Morita, A. et al. 2020, in preparation

Moscadelli, L., Cesaroni, R., Rioja, M. J., Dodson, R., & Reid, M. J. 2011, *A&A*, 526, A66

Motogi, K., Sorai, K., Habe, A., Honma, M., Kobayashi, H., & Sato, K. 2011, *PASJ*, 63, 31

Motogi, K. et al. 2016, *PASJ*, 68, 69

Müller, H. S. P., Thorwirth, S., Roth, D. A., & Winnewisser, G. 2001, *A&A*, 370, L49

Nagayama, T. et al. 2015a, *PASJ*, 67, 65

Nagayama, T. et al. 2015b, *PASJ*, 67, 66

Nagayama, T. et al. 2020a, *PASJ*, submitted to *PASJ*

Nagayama, T. et al. 2020b, *PASJ*, submitted to *PASJ*

Nagayama, T., Omodaka, T., Handa, T., Honma, M., Kobayashi, H., Kawaguchi, N., & Ueno, Y. 2011a, *PASJ*, 63, 719

Nagayama, T., Omodaka, T., Nakagawa, A., Handa, T., Honma, M., Kobayashi, H., Kawaguchi, N., & Miyaji, T. 2011b, *PASJ*, 63, 23

Nakagawa, A., Kurayama, T., Matsui, M., Omodaka, T., Honma, M., Shibata, K. M., Sato, K., & Jike, T. 2016, *PASJ*, 68, 78

Nakagawa, A. et al. 2014, *PASJ*, 66, 101

Nakagawa, A. et al. 2008, *PASJ*, 60, 1013

Nakagawa, A. et al. 2020, in preparation

Nakanishi, H. et al. 2015, *PASJ*, 67, 68

Nakanishi, H. et al. 2020, in preparation

Niinuma, K. et al. 2011, *PASJ*, 63, 9

Nyu, D. et al. 2011, *PASJ*, 63, 63

Ogbodo, C. S. et al. 2017, *MNRAS*, 469, 4788

Oh, C. S., Kobayashi, H., Honma, M., Hirota, T., Sato, K., & Ueno, Y. 2010, *PASJ*, 62, 101

Omodaka, T. et al. 2020, in preparation

Ooyama, M. et al. 2020, in preparation

Ortiz-León, G. N. et al. 2017, *ApJ*, 834, 141

Ortiz-León, G. N. et al. 2018a, *ApJ*, 865, 73

Ortiz-León, G. N. et al. 2018b, *ApJL*, 869, L33

Oyama, T. et al. 2016, *PASJ*, 68, 105

Petrov, L., Honma, M., & Shibata, S. M. 2012, *AJ*, 143, 35

Petrov, L., Hirota, T., Honma, M., Shibata, K. M., Jike, T., & Kobayashi, H. 2007, *AJ*, 133, 2487

Pickett, H. M., Poynter, R. L., Cohen, E. A., Delitsky, M. L., Pearson, J. C., & Müller, H. S. P. 1998, *J. Quant. Spectrosc. Radiat. Transfer*, 60, 883

Quiroga-Nuñez, L. H., Immer, K., van Langevelde, H. J., Reid, M. J., & Burns, R. A. 2019, *A&A*,

- Reid, M. J., & Honma, M. 2014a, *ARA&A*, 52, 339
- Reid, M. J. et al. 2014b, *ApJ*, 783, 130
- Reid, M. J., & Brunthaler, A. 2004, *ApJ*, 616, 872
- Reid, M. J., & Brunthaler, A. 2020, arXiv e-prints, arXiv:2001.04386
- Reid, M. J., Menten, K. M., Brunthaler, A., Zheng, X. W., Moscadelli, L., & Xu, Y. 2009a, *ApJ*, 693, 397
- Reid, M. J. et al. 2009b, *ApJ*, 700, 137
- Reid, M. J., Menten, K. M., Zheng, X. W., Brunthaler, A., & Xu, Y. 2009c, *ApJ*, 705, 1548
- Reid, M. J. et al. 2019, *ApJ*, 885, 131
- Reid, M. J., Schneps, M. H., Moran, J. M., Gwinn, C. R., Genzel, R., Downes, D., & Roennaeng, B. 1988, *ApJ*, 330, 809
- Rygl, K. L. J., Brunthaler, A., Reid, M. J., Menten, K. M., van Langevelde, H. J., & Xu, Y. 2010, *A&A*, 511, A2
- Sakai, D., Oyama, T., Nagayama, T., Honma, M., & Kobayashi, H. 2017, *PASJ*, 69, 64
- Sakai, D. et al. 2020a, in preparation
- Sakai, N., Honma, M., Nakanishi, H., Sakanoue, H., Kurayama, T., Shibata, K. M., & Shizugami, M. 2012, *PASJ*, 64, 108
- Sakai, N. et al. 2015, *PASJ*, 67, 69
- Sakai, N., Reid, M. J., Menten, K. M., Brunthaler, A., & Dame, T. M. 2019, *ApJ*, 876, 30
- Sakai, N., Sato, M., Motogi, K., Nagayama, T., Shibata, K. M., Kanaguchi, M., & Honma, M. 2014, *PASJ*, 66, 3
- Sakai, N. et al. 2020b, *PASJ*, in press
- Sakai, N. et al. 2020c, in preparation
- Sandstrom, K. M., Peek, J. E. G., Bower, G. C., Bolatto, A. D., & Plambeck, R. L. 2007, *ApJ*, 667, 1161
- Sanna, A., Reid, M. J., Dame, T. M., Menten, K. M., & Brunthaler, A. 2017, *Science*, 358, 227
- Sato, M. et al. 2014, *ApJ*, 793, 72
- Sato, M. et al. 2008, *PASJ*, 60, 975
- Sato, M., Hirota, T., Reid, M. J., Honma, M., Kobayashi, H., Iwadate, K., Miyaji, T., & Shibata, K. M. 2010, *PASJ*, 62, 287
- Schönrich, R., Binney, J., & Dehnen, W. 2010, *MNRAS*, 403, 1829
- Shiozaki, S., Imai, H., Tafuya, D., Omodaka, T., Hirota, T., Honma, M., Matsui, M., & Ueno, Y. 2011, *PASJ*, 63, 1219

Sudou, H. et al. 2019, PASJ, 71, 16
Tafoya, D. et al. 2011, PASJ, 63, 71
Ulich, B. L., & Haas, R. W. 1976, ApJS, 30, 247
Urago, R. et al. 2020, in preparation
Wu, Y. W. et al. 2019, ApJ, 874, 94
Wu, Y. W. et al. 2014, A&A, 566, A17
Xu, S., Zhang, B., Reid, M. J., et al. 2019, ApJ, 875, 114
Xu, Y. et al. 2013, ApJ, 769, 15
Xu, Y., Moscadelli, L., Reid, M. J., Menten, K. M., Zhang, B., Zheng, X. W., & Brunthaler, A. 2011, ApJ, 733, 25
Xu, Y., Reid, M. J., Zheng, X. W., & Menten, K. M. 2006, Science, 311, 54
Yamauchi, A., Yamashita, K., Honma, M., Sunada, K., Nakagawa, A., & Ueno, Y. 2016, PASJ, 68, 60
Zhang, B., Reid, M. J., Menten, K. M., & Zheng, X. W. 2012, ApJ, 744, 23
Zhang, B., Reid, M. J., Menten, K. M., Zheng, X. W., Brunthaler, A., Dame, T. M., & Xu, Y. 2013, ApJ, 775, 79
Zhang, B., Zheng, X. W., Reid, M. J., Menten, K. M., Xu, Y., Moscadelli, L., & Brunthaler, A. 2009, ApJ, 693, 419
Zucker, C., Speagle, J. S., Schlafly, E. F., Green, G. M., Finkbeiner, D. P., Goodman, A. A., & Alves, J. 2019, ApJ, 879, 125

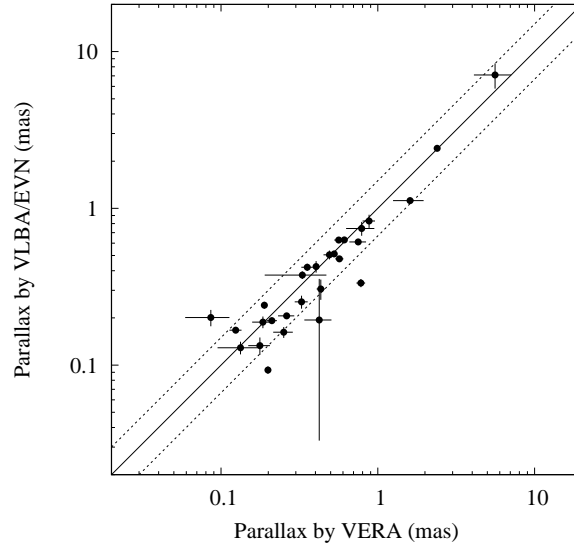


Fig. 1. Comparison of parallaxes from VERA and VLBA/EVN. A solid line indicates the VERA parallaxes equal to those of VLBA/EVN while dashed lines show their differences by factors of 1/1.5 and 1.5.

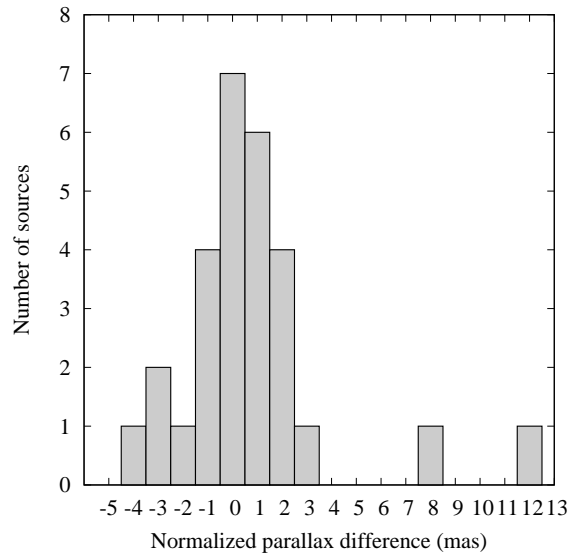


Fig. 2. Histogram of the normalized parallax differences scaled by their joint uncertainties. See definition in equation 1. Each bin has the central value of integer with its width of 1 (e.g. $\Delta\pi/\sigma_{\Delta\pi} = 0.0 \pm 0.5, 1.0 \pm 0.5, -1.0 \pm 0.5, \dots$).

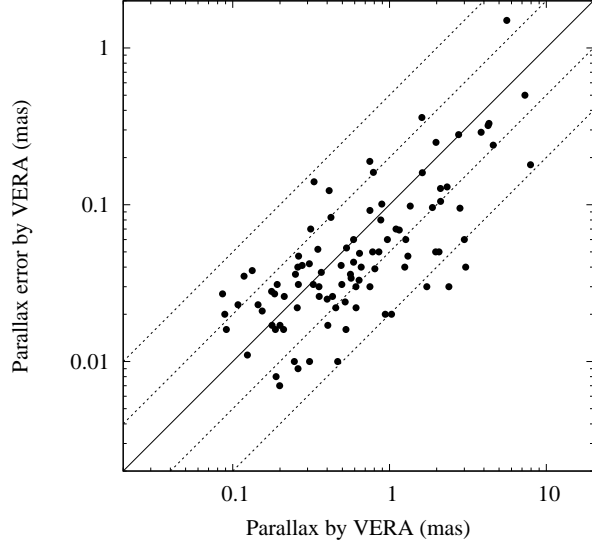


Fig. 3. Parallax values and their errors obtained from the VERA astrometry. A solid line indicates the parallax errors of 10%, while dashed lines represent the errors of 50%, 20%, 5%, and 2%.

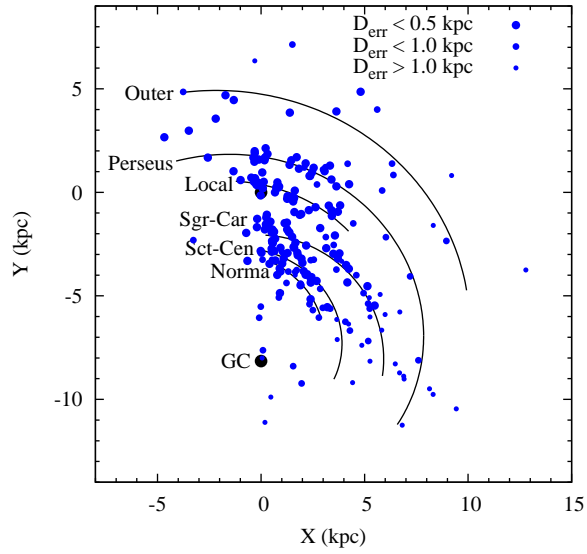


Fig. 4. Distributions of the maser sources on the face-on view of the Galaxy. Solid line show the spiral arm structure identified by the BeSSeL results (Reid et al. 2019).

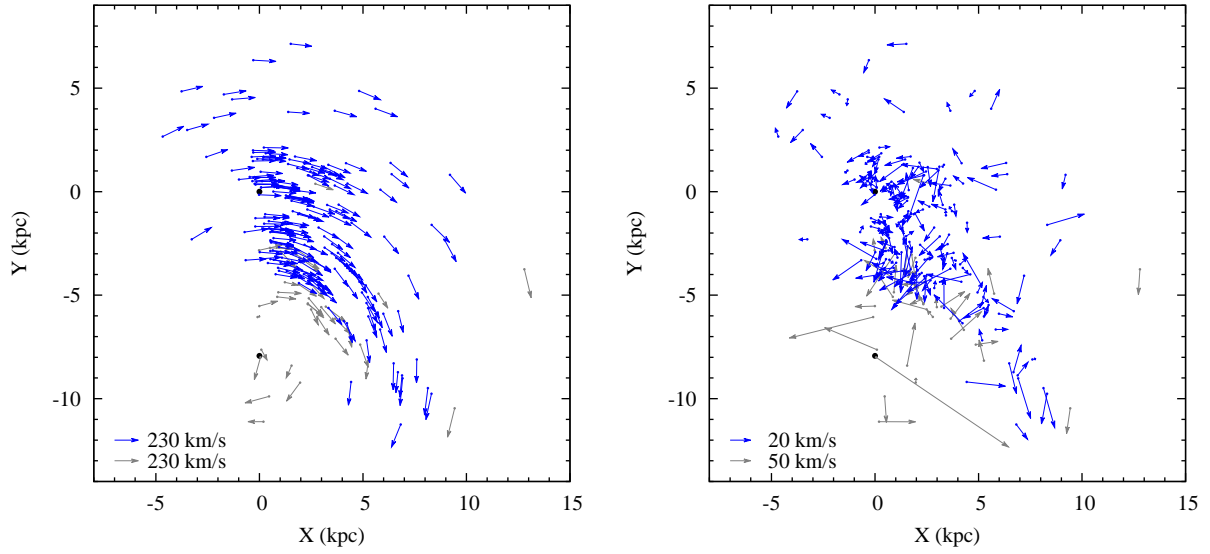


Fig. 5. Galactic rotation motions (left) and peculiar motions (right) of the maser sources. Gray symbols indicate the outliers with $R < 4$ kpc or the peculiar motion of $V > 50$ km s $^{-1}$, which are removed from the MCMC analysis (see text). Rest of the sources are plotted in the blue symbols. Number of blue and gray symbols are 189 and 35, respectively (total 224 sources). The Galactic parameters for the model with the power-law rotation curve (Table 3) and the Solar motion of $(U_{\odot}, V_{\odot}, W_{\odot}) = (11.1, 12.24, 7.25)$ in km s $^{-1}$ (Schönrich et al. 2010) are employed to plot the vectors.

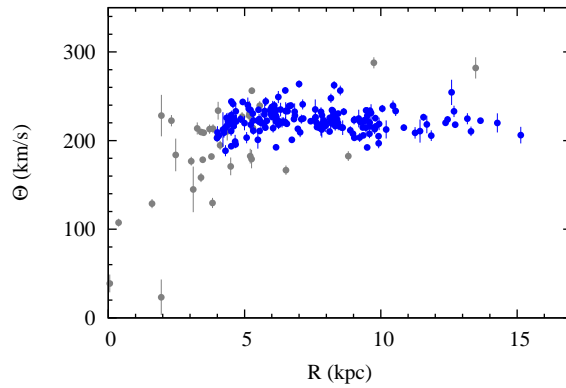


Fig. 6. Rotation curve of the Galaxy. The blue and gray symbols are the same as in Figure 5.

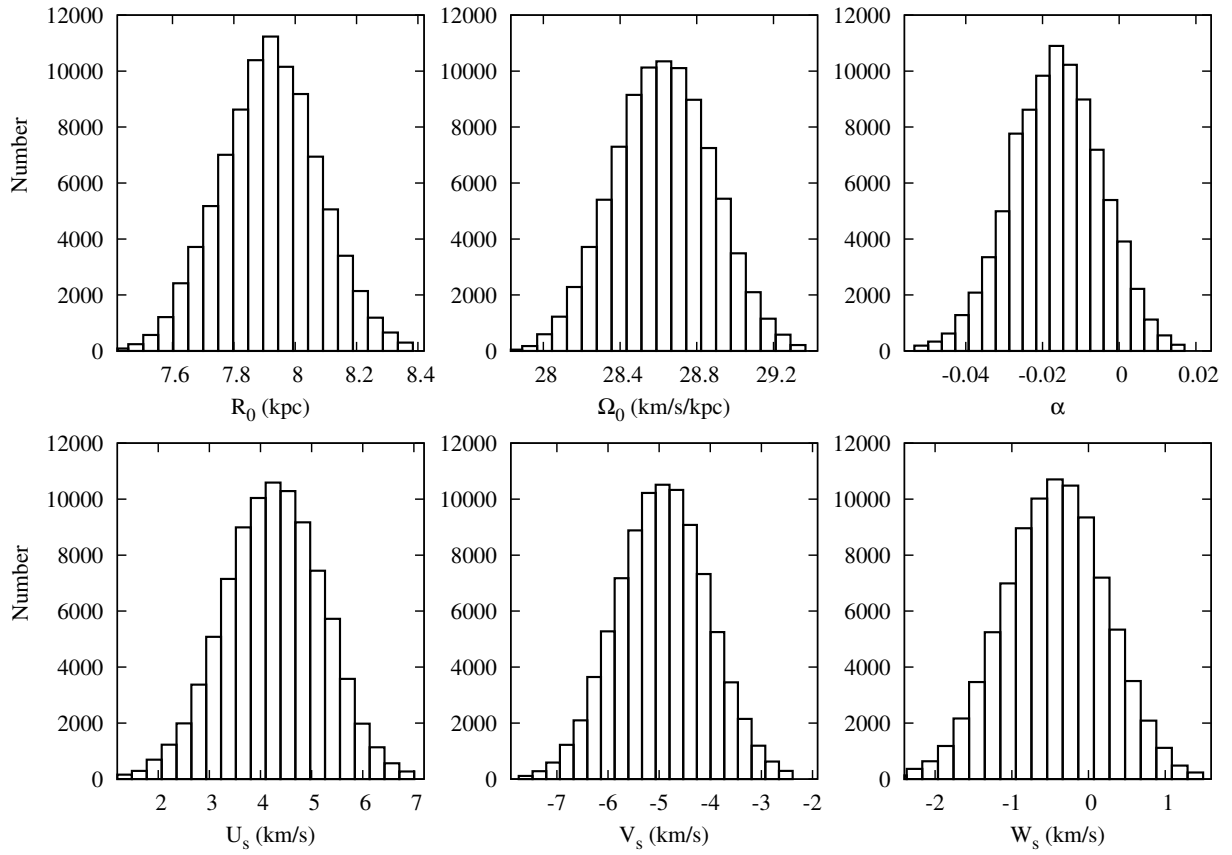


Fig. 7. Posterior probability distribution for the Galactic parameters in the case of the power law model. From top-left to bottom-right, each panel shows a plot for R_0 , Ω_0 , α , U_s , V_s , and W_s .

Table 1. Astrometry results from VERA

NAME	RA(J2000) (h:m:s)	Dec(J2000) (d:m:s)	l (deg)	b (deg)	π_{VERA} (mas)	σ_{VERA} (mas)	μ_x (mas yr ⁻¹)	$\Delta\mu_x$ (mas yr ⁻¹)	μ_y (mas yr ⁻¹)	$\Delta\mu_y$ (mas yr ⁻¹)	v_{lsr} (km s ⁻¹)	Δv_{lsr} (km s ⁻¹)	Type	Reference
SY Scl	00 07 36.2476	-25 29 40.028	039.91	-80.04	0.75	0.03	+5.57	0.04	-7.32	0.12	+22.0	5.0	AGB	Nyu et al. (2011)
IRAS 00259+5625	00 28 43.5075	+56 41 56.868	119.80	-06.03	0.412	0.123	-2.48	0.32	-2.85	0.65	-38.3	3.1	SFR	Sakai et al. (2014)
NGC 281	00 52 24.7008	+56 33 50.527	123.06	-06.30	0.355	0.030	-2.63	0.05	-1.86	0.08	-30.0	5.0	SFR	Sato et al. (2008)
G125.51+02.03	01 15 40.8027	+64 46 40.766	125.51	+02.03	0.145	0.023	-1.20	0.21	-0.33	0.27	-57.0	9.0	SFR	Koide et al. (2019), Sakai et al. (2020b) ^a
W3(H ₂ O)	02 27 04.6800	+61 52 24.566	133.94	+01.06	0.527	0.016	+0.27	0.29	-1.24	0.15	-55.6	1.2	SFR	Matsumoto et al. (2011), Nagayama et al. (2020b) ^a
G135.28+02.80	02 43 28.5825	+62 57 08.390	135.28	+02.80	0.124	0.011	-0.45	0.20	+0.09	0.16	-72.9	1.6	SFR	Nagayama et al. (2020a)
G137.07+03.00	02 58 13.1793	+62 20 32.915	137.07	+03.00	0.187	0.016	-0.57	0.16	-0.01	0.16	-50.1	0.4	SFR	Nagayama et al. (2020a)
L1448C	03 25 38.8784	+30 44 05.252	157.57	-21.94	4.31	0.33	+21.90	0.70	-23.10	3.30	+5.0	5.0	SFR	Hirota et al. (2011)
NGC 1333 SVS13	03 29 03.7247	+31 16 03.802	158.35	-20.56	4.25	0.32	+14.25	2.58	-9.95	0.74	+8.0	5.0	SFR	Hirota et al. (2008a)
V637 Per	03 54 02.2577	+36 32 17.926	159.10	-13.20	0.94	0.02	-0.61	0.43	-0.90	0.37	-97.8	0.9	AGB	Present paper
L1482	04 30 27.4008	+35 09 17.649	165.47	-09.05	1.879	0.096	+3.07	0.06	-8.60	0.04	+1.0	5.0	SFR	Omodaka et al. (2020)
BX Eri	04 40 32.7762	-14 12 02.710	211.48	-35.33	2.116	0.105	+6.77	0.35	-10.79	0.25	-0.3	0.1	AGB	Present paper
T Lep	05 04 50.8430	-21 54 16.505	222.67	-32.71	3.06	0.04	+14.60	0.50	-35.43	0.79	-27.6	5.0	AGB	Nakagawa et al. (2014)
IRAS 05137+3919	05 17 13.7410	+39 22 19.880	168.06	+00.82	0.086	0.027	+0.30	0.27	-0.89	0.73	-27.0	5.0	SFR	Honma et al. (2011)
BW Cam	05 19 52.1643	+63 15 54.684	143.43	+20.09	0.749	0.189	+7.55	1.19	-19.63	0.81	+42.0	0.7	AGB	Present paper
IRAS 05168+3634	05 20 22.0700	+36 37 56.630	170.66	-00.25	0.532	0.053	+0.23	1.07	-3.14	0.28	-15.5	1.9	SFR	Sakai et al. (2012)
AFGL 5142	05 30 48.0173	+33 47 54.568	174.20	-00.07	0.467	0.010	+0.32	0.27	-0.22	0.47	-2.0	5.0	SFR	Burns et al. (2017)
Orion KL	05 35 14.5050	-05 22 30.450	209.00	-19.38	2.39	0.03	+9.56	0.10	-3.83	0.15	+3.0	5.0	SFR	Hirota et al. (2007), Kim et al. (2008) ^a , Nagayama et al. (2020b)
WB 673	05 38 00.3500	+35 58 58.400	173.17	+02.36	0.590	0.043	+0.01	0.03	-3.40	0.09	-10.4	0.2	SFR	Present paper
RW Lep	05 38 52.7260	-14 02 27.180	217.78	-22.30	1.62	0.16	+15.80	2.10	-31.20	2.10	-59.0	1.0	AGB	Kamezaki et al. (2014b)
L1641 S3	05 39 56.0431	-07 30 27.988	211.57	-19.29	2.114	0.127	-11.68	0.67	-7.74	0.36	+6.8	4.2	SFR	Present paper
S235AB MIR	05 40 53.3800	+35 41 48.500	173.72	+02.70	0.639	0.033	+0.08	0.12	-2.41	0.14	-17.0	5.0	SFR	Burns et al. (2015)
B35	05 44 29.2483	+09 08 52.121	196.93	-10.40	1.98	0.25	-2.30	0.53	-5.31	0.59	+12.0	1.0	SFR	Present paper
BX Cam	05 46 44.3251	+69 58 24.408	143.43	+20.09	1.73	0.03	+13.48	0.14	-34.30	0.18	0.0	5.0	AGB	Matsuno et al. (2020)
G192.16-03.81	05 58 13.5300	+16 31 58.900	192.16	-03.81	0.66	0.04	+0.69	0.15	-1.57	0.15	+5.7	5.0	SFR	Shiozaki et al. (2011)
IRAS 06058+2138	06 08 53.4938	+21 38 30.741	188.94	+00.88	0.569	0.034	+1.06	0.18	-2.77	0.34	+3.0	5.0	SFR	Oh et al. (2010)
IRAS 06061+2151	06 09 06.9746	+21 50 41.405	188.79	+01.03	0.496	0.031	-0.10	0.10	-3.91	0.07	-1.6	0.2	SFR	Niinuma et al. (2011)
HH 12-15	06 10 50.1400	-06 11 45.600	213.88	-11.84	1.61	0.36	-0.36	1.68	+3.17	0.47	+11.3	2.0	SFR	Present paper
S255 IR-SMA1	06 12 54.0064	+17 59 22.959	192.60	-00.05	0.563	0.036	-0.13	0.20	-0.06	0.27	+5.3	5.0	SFR	Burns et al. (2016)
S269	06 14 37.0800	+13 49 36.700	196.45	-01.67	0.189	0.008	-0.42	0.20	-0.12	0.20	+18.0	5.0	SFR	Honma et al. (2007) ^a , Asaki et al. (2014)
G200.08-01.63	06 21 47.5742	+10 39 22.811	200.08	-01.63	0.200	0.017	+0.32	0.14	-0.14	0.16	+36.3	0.6	SFR	Nagayama et al. (2020a)
U Lyn	06 40 46.4853	+59 52 01.490	155.66	+21.94	1.27	0.06	+0.80	0.57	-6.00	0.56	-13.0	3.0	AGB	Kamezaki et al. (2016a)
NGC 2264	06 41 09.8600	+09 29 14.700	203.32	+02.05	1.356	0.098	-1.08	0.58	-5.92	3.06	+7.0	3.0	SFR	Kamezaki et al. (2014a)
WB 886	06 47 13.3000	+00 26 05.920	212.06	-00.74	0.349	0.052	-0.40	0.94	+0.37	0.33	+45.0	3.0	SFR	Nakanishi et al. (2020)
NSV 17351	07 07 49.3869	-10 44 05.998	224.34	-01.29	0.247	0.010	-1.19	0.11	+1.30	0.19	-50.1	1.9	AGB	Morita et al. (2020)
VY CMa	07 22 58.3291	-25 46 03.141	239.35	-05.06	0.88	0.08	-2.09	0.16	+1.02	0.61	+20.0	5.0	RSG	Choi et al. (2008)
OZ Gem	07 33 57.7500	+30 30 37.799	188.80	+21.90	0.806	0.039	-1.97	0.32	-8.69	0.21	+8.7	1.4	AGB	Urago et al. (2020)
QX Pup	07 42 16.9470	-14 42 50.200	231.84	+04.22	0.61	0.03	-4.76	0.37	-0.94	0.62	+33.0	5.0	AGB	Ooyama et al. (2020)
IRAS 07427-2400	07 44 51.9200	-24 07 41.500	240.31	+00.07	0.185	0.027	-1.79	0.32	+2.60	0.17	+66.4	5.0	SFR	Sakai et al. (2015)

Table 1. (Continued)

NAME	RA(J2000) (h:m:s)	Dec(J2000) (d:m:s)	l (deg)	b (deg)	π_{VERA} (mas)	σ_{VERA} (mas)	μ_x (mas yr ⁻¹)	$\Delta\mu_x$ (mas yr ⁻¹)	μ_y (mas yr ⁻¹)	$\Delta\mu_y$ (mas yr ⁻¹)	v_{lsr} (km s ⁻¹)	Δv_{lsr} (km s ⁻¹)	Type	Reference
HU Pup	07 55 40.1843	-28 38 54.608	245.44	-00.15	0.308	0.042	-1.16	0.15	+3.69	0.20	+43.9	0.6	AGB	Present paper
R Cnc	08 16 33.8243	+11 43 34.518	211.75	+24.14	3.84	0.29	+1.24	0.34	-11.57	0.97	+16.9	5.0	AGB	Present paper
X Hya	09 35 30.2650	-14 41 28.639	248.15	+26.70	2.07	0.05	-51.37	0.97	-15.02	1.47	+27.3	5.0	AGB	Present paper
R UMa	10 44 38.4283	+68 46 32.344	138.36	+44.36	1.97	0.05	-40.77	0.39	-24.75	0.38	+40.5	1.0	AGB	Nakagawa et al. (2016)
W Leo	10 53 37.4325	+13 42 54.367	233.02	+59.43	1.03	0.02	-6.84	0.09	-8.65	0.08	+46.7	0.2	AGB	Present paper
HS UMa	11 35 30.6878	+34 52 04.006	182.78	+72.02	2.816	0.095	-11.48	0.17	-10.86	0.65	+1.6	0.3	AGB	Present paper
S Crt	11 52 45.9697	-07 35 48.096	278.59	+52.48	2.33	0.13	-3.17	0.22	-5.41	0.22	+37.9	5.0	AGB	Nakagawa et al. (2008)
R Hya	13 29 42.7819	-23 16 52.775	314.22	+38.75	7.93	0.18	-53.79	1.05	+16.15	1.83	-8.5	5.0	AGB	Present paper
RX Boo	14 24 11.6206	+25 42 12.909	034.28	+69.21	7.31	0.50	+24.55	1.06	-49.67	2.38	+1.0	5.0	AGB	Kamezaki et al. (2012)
FX Boo	15 08 25.7530	+09 36 18.390	011.03	+53.27	0.97	0.06	+6.81	0.14	+1.01	0.12	+7.5	1.0	AGB	Kamezaki et al. (2016b)
Y Lib	15 11 41.2990	-06 00 41.462	353.83	+42.59	0.855	0.050	-10.15	2.39	-15.02	4.26	+14.4	1.1	AGB	Chibueze et al. (2019)
S Ser	15 21 39.5334	+14 18 53.107	020.50	+52.79	1.25	0.04	-2.56	1.42	+5.20	2.31	+25.1	5.0	AGB	Present paper
IRAS 16293-2422	16 32 22.8500	-24 28 36.400	353.94	-15.84	5.6	1.5	-20.60	0.70	-32.40	2.00	+3.0	5.0	SFR	Imai et al. (2007)
NGC 6334I(N)	17 20 55.1920	-35 45 03.770	351.44	+00.65	0.789	0.161	-2.88	0.30	+3.23	0.39	-2.8	0.5	SFR	Chibueze et al. (2014a)
G353.27+00.64	17 26 01.5883	-34 15 14.903	353.27	+00.64	0.59	0.06	+0.47	0.07	+0.99	1.04	-5.0	5.0	SFR	Motogi et al. (2016)
G359.62-00.25	17 45 39.0908	-29 20 26.294	359.62	-00.25	0.33	0.14	+1.31	0.33	-2.41	0.87	-80.0	5.0	SFR	Iwata et al. (2017)
Sgr B2	17 47 20.1817	-28 23 03.889	000.67	-00.03	0.133	0.038	-1.83	0.21	-3.70	0.09	+62.0	5.0	SFR	Sakai et al. (2020a)
Sgr D	17 48 48.5450	-28 01 26.290	001.15	-00.12	0.423	0.083	-0.76	0.15	-2.88	0.34	-18.0	5.0	SFR	Sakai et al. (2017)
G005.88-00.39	18 00 30.3100	-24 04 04.500	005.88	-00.39	0.78	0.05	-0.17	0.60	-0.95	0.48	+9.0	3.0	SFR	Motogi et al. (2011)
G007.47+00.06	18 02 13.1790	-22 27 58.960	007.47	+00.06	—	—	-2.42	0.09	-4.39	0.08	-15.0	5.0	SFR	Yamauchi et al. (2016) ^b
G014.33-00.64	18 18 54.6532	-16 47 50.077	014.33	-00.64	0.893	0.101	+0.95	2.00	-2.50	2.00	+22.0	5.0	SFR	Sato et al. (2010)
M17	18 20 23.0160	-16 11 48.030	015.03	-00.67	0.491	0.041	-0.51	0.21	-2.04	0.21	+20.0	5.0	SFR	Chibueze et al. (2016)
G021.88+00.02	18 31 01.7490	-09 49 01.130	021.88	+00.01	—	—	-3.30	0.06	-5.33	0.22	+26.9	0.4	SFR	Present paper ^b
IRAS 18286-0959	18 31 22.9340	-09 57 21.700	021.80	-00.13	0.277	0.041	-3.20	0.30	-7.20	0.20	+60.0	5.0	AGB	Imai et al. (2013)
G034.39+00.22	18 53 18.7700	+01 24 08.800	034.39	+00.22	0.643	0.049	-0.25	0.80	—	—	+58.0	5.0	SFR	Kurayama et al. (2011) ^b
S76E	18 56 11.4413	+07 53 17.608	040.50	+02.54	0.521	0.024	-0.89	0.34	-2.27	0.56	+31.9	1.7	SFR	Chibueze et al. (2017)
G037.50+00.53	18 57 53.3876	+04 18 17.394	037.50	+00.53	0.091	0.016	-2.74	0.18	-5.49	0.10	+10.7	2.6	SFR	Nagayama et al. (2020a)
G037.82+00.41	18 58 53.8800	+04 32 15.004	037.82	+00.41	0.089	0.020	-2.73	0.12	-5.53	0.12	+17.5	0.8	SFR	Nagayama et al. (2020a)
W48A	19 01 45.5423	+01 13 32.573	035.20	-01.74	0.433	0.026	-0.05	0.81	-3.51	0.38	+41.9	1.4	SFR	Chibueze et al. (2020)
G044.31+00.04	19 12 15.7930	+10 07 53.085	044.31	+00.04	0.192	0.031	-3.36	0.05	-6.92	0.06	+57.8	0.5	SFR	Present paper
G048.60+00.02	19 20 31.1772	+13 55 25.257	048.60	+00.02	0.199	0.007	-2.76	0.04	-5.28	0.11	+19.0	1.0	SFR	Nagayama et al. (2011a)
G048.99-00.30	19 22 26.1348	+14 06 39.133	048.99	-00.30	0.178	0.017	-2.16	0.09	-5.87	0.17	+66.3	0.3	SFR	Nagayama et al. (2015a)
G049.19-00.33	19 22 57.7705	+14 16 09.969	049.19	-00.33	0.211	0.016	-3.21	0.07	-5.08	0.25	+69.9	0.5	SFR	Nagayama et al. (2015a)
IRAS 19213+1723	19 23 37.3229	+17 29 10.479	052.10	+01.04	0.251	0.036	-2.53	0.04	-6.07	0.05	+41.7	5.0	SFR	Oh et al. (2010)
K3-35	19 27 44.0230	+21 30 03.440	056.10	+02.09	0.260	0.040	-3.34	0.10	-5.93	0.07	+26.0	5.0	AGB	Tafoya et al. (2011)
IRAS 19312+1950	19 33 24.2430	+19 56 55.650	055.37	+00.19	0.263	0.047	-2.61	0.47	-6.73	0.14	+36.0	1.0	SFR	Imai et al. (2011)
G061.48+00.10	19 46 47.9175	+25 12 52.698	061.48	+00.10	0.454	0.022	-1.31	0.16	-6.39	0.34	+41.7	6.2	SFR	Present paper
SY Aql	20 07 05.4083	+12 57 06.219	053.37	-10.31	1.10	0.07	+12.26	0.11	-15.93	0.22	-44.8	5.0	AGB	Present paper
IRAS 20056+3350	20 07 31.2586	+33 59 41.477	071.31	+00.83	0.213	0.026	-2.62	0.33	-5.65	0.52	+9.4	5.0	SFR	Burns et al. (2014a)
ON1	20 10 09.2045	+31 31 36.101	069.54	-00.97	0.404	0.017	-3.10	0.18	-4.70	0.24	+12.0	1.0	SFR	Nagayama et al. (2011b)
IRAS 20126+4104	20 14 26.0218	+41 13 32.674	078.12	+03.63	0.750	0.092	-4.15	0.51	-4.07	0.51	-3.5	4.0	SFR	Nagayama et al. (2015b)
IRAS 20143+3634	20 16 13.3617	+36 43 33.920	074.57	+00.85	0.367	0.037	-2.99	0.16	-4.37	0.43	-1.0	1.0	SFR	Burns et al. (2014b)
ON2N	20 21 44.0123	+37 26 37.484	075.78	+00.34	0.261	0.009	-2.79	0.13	-4.66	0.17	+0.0	1.0	SFR	Ando et al. (2011)
IRAS 20231+3430	20 25 07.8013	+34 50 34.733	074.04	-01.71	0.611	0.022	-3.79	0.18	-4.88	0.25	+6.0	5.0	SFR	Ogbodo et al. (2017)

Table 1. (Continued)

NAME	RA(J2000) (h:m:s)	Dec(J2000) (d:m:s)	l (deg)	b (deg)	π_{VERA} (mas)	σ_{VERA} (mas)	μ_x (mas yr ⁻¹)	$\Delta\mu_x$ (mas yr ⁻¹)	μ_y (mas yr ⁻¹)	$\Delta\mu_y$ (mas yr ⁻¹)	v_{lsr} (km s ⁻¹)	Δv_{lsr} (km s ⁻¹)	Type	Reference
IRAS 20255+4032	20 27 20.2734	+40 42 34.648	079.09	+01.33	0.118	0.035	-2.49	0.13	-3.36	0.23	-18.2	5.0	SFR	Sakai et al. (2020c)
G080.70+00.70	20 35 09.1650	+41 38 20.260	080.70	+00.70	0.258	0.022	-3.18	0.09	-5.09	0.07	-2.3	0.7	SFR	Present paper
G095.05+03.97	21 15 55.6798	+54 43 31.328	095.05	+03.97	0.108	0.023	-2.44	0.21	-2.63	0.17	-87.0	5.0	SFR	Sakai et al. (2020b) ^a , Nakanishi et al. (2020)
G097.53+03.18	21 32 12.4400	+55 53 49.600	097.53	+03.18	0.177	0.028	-2.64	0.20	-2.38	0.22	-73.0	5.0	SFR	Sakai et al. (2020b) ^a , Nakanishi et al. (2020)
IRAS 21379+5106	21 39 40.5500	+51 20 34.000	095.29	-00.93	0.262	0.031	-2.74	0.08	-2.87	0.18	-42.3	0.2	SFR	Nakanishi et al. (2015)
AFGL 2789	21 39 58.2717	+50 14 21.014	094.60	-01.79	0.326	0.031	-2.20	0.08	-3.77	0.15	-44.0	5.0	SFR	Oh et al. (2010)
G102.35+03.64	21 57 25.1841	+59 21 56.614	102.35	+03.64	0.154	0.021	-2.53	0.33	-2.14	0.33	-88.0	5.0	SFR	Sakai et al. (2020b) ^a , Nakanishi et al. (2020)
SV Peg	22 05 42.0850	+35 20 54.536	088.72	-16.29	3.00	0.06	+11.59	0.54	-8.63	0.44	+3.9	5.0	AGB	Sudou et al. (2019)
S140	22 19 17.4657	+63 18 39.851	106.79	+05.31	1.154	0.069	-6.16	0.12	-4.74	0.11	-6.1	5.0	SFR	Present paper
IRAS 22198+6336	22 21 26.7279	+63 51 37.924	107.29	+05.63	1.309	0.047	-2.47	1.40	+0.26	1.40	-11.0	5.0	SFR	Hirota et al. (2008b)
IRAS 22480+6002	22 49 58.8760	+60 17 56.650	108.43	-00.89	0.400	0.025	-2.58	0.33	-1.91	0.17	-50.8	3.5	SFR	Imai et al. (2012)
IRAS 22555+6213	22 57 29.8090	+62 29 46.850	110.20	+02.48	0.314	0.070	-2.04	0.05	-0.66	0.06	-63.0	1.0	SFR	Chibueze et al. (2014b)
IRAS 23004+5642	23 02 32.0800	+56 57 51.400	108.47	-02.81	0.309	0.010	-2.45	1.00	-3.00	0.70	-54.0	5.0	SFR	Nakanishi et al. (2020)
R Peg	23 06 39.1652	+10 32 36.078	085.41	-44.56	2.76	0.28	+3.60	1.53	-6.44	0.92	+22.5	5.0	AGB	Present paper
R Aqr	23 43 49.4616	-15 17 04.202	066.52	-70.33	4.59	0.24	+37.13	0.47	-28.62	0.44	-21.5	5.0	AGB	Kamohara et al. (2010), Min et al. (2014) ^a
PZ Cas	23 44 03.2816	+61 47 22.187	115.06	-00.05	0.356	0.026	-3.70	0.20	-2.00	0.30	-36.2	0.7	RSG	Kusuno et al. (2013)

a: If there are multiple references, the data with smaller parallax errors noted with ^a is employed.

b: Their parallax and/or proper motions cannot be determined.

Table 2. Parallaxes from VERA and VLBA/EVN and their differences

Name	π_{VERA} (mas)	π_{VLBA} (mas)	$\pi_{\text{VERA}} - \pi_{\text{VLBA}}$ (mas)	$\Delta\pi/\sigma_{\Delta\pi}$	References for VLBA/EVN
NGC 281/NGC 281-W	0.355±0.030	0.421±0.022	-0.07 ± 0.04	-1.77	Rygl et al. (2010)
W3(H ₂ O)/W3(OH)	0.527±0.016	0.512±0.010	0.02 ± 0.02	0.79	Xu et al. (2006) ^a , Hachisuka et al. (2006)
G135.28+02.80	0.124±0.011	0.167±0.006	-0.04 ± 0.01	-3.43	Hachisuka et al. (2009)
IRAS 05137+3919	0.086±0.027	0.201±0.024	-0.12 ± 0.04	-3.18	Hachisuka et al. (2015)
Orion KL	2.39±0.03	2.415±0.040	-0.02 ± 0.05	-0.50	Menten et al. (2007)
IRAS 06058+2138	0.569±0.034	0.476±0.006	0.09 ± 0.03	2.69	Reid et al. (2009a) ^a , Sakai et al. (2019)
HH 12-15	1.61±0.36	1.12±0.05	0.48 ± 0.36	1.35	Dzib et al. (2016)
S255 IR-SMA1	0.563±0.036	0.628±0.027	-0.07 ± 0.04	-1.44	Rygl et al. (2010)
S269	0.189±0.008	0.241±0.012	-0.05 ± 0.01	-3.61	Quiroga-Nuñez et al. (2019)
VY CMa	0.88±0.08	0.83±0.08	0.05 ± 0.11	0.44	Zhang et al. (2012)
IRAS 07427-2400	0.185±0.027	0.188±0.016	-0.00 ± 0.03	-0.10	Choi et al. (2014)
IRAS 16293-2422	5.6±1.5	7.1±1.3	-1.50 ± 1.98	-0.76	Dzib et al. (2018)
NGC 6334I(N)	0.789±0.161	0.744±0.076	0.05 ± 0.18	0.25	Wu et al. (2014)
G359.62-00.25	0.33±0.14	0.375±0.021	-0.04 ± 0.14	-0.32	Reid et al. (2019)
Sgr B2	0.133±0.038	0.129±0.012	0.00 ± 0.04	0.10	Reid et al. (2009c)
Sgr D	0.423±0.083	0.194±0.161	0.23 ± 0.18	1.26	Reid et al. (2019)
G005.88-00.39	0.78±0.05	0.334±0.020	0.45 ± 0.05	8.28	Sato et al. (2014)
M17	0.491±0.041	0.505±0.033	-0.01 ± 0.05	-0.27	Xu et al. (2011)
W48A	0.433±0.026	0.306±0.045	0.13 ± 0.05	2.44	Zhang et al. (2009)
G048.60+00.02	0.199±0.007	0.093±0.005	0.11 ± 0.01	12.32	Zhang et al. (2013)
G049.19-00.33	0.211±0.016	0.192±0.009	0.02 ± 0.02	1.03	Wu et al. (2014)
IRAS 19213+1723	0.251±0.036	0.162±0.013	0.09 ± 0.04	2.33	Wu et al. (2019)
ON1	0.404±0.017	0.425±0.036	-0.02 ± 0.04	-0.53	Rygl et al. (2010), Xu et al. (2013) ^a
IRAS 20126+4104	0.750±0.092	0.61±0.02	0.14 ± 0.09	1.49	Moscadelli et al. (2011)
IRAS 20231+3430	0.611±0.022	0.629±0.017	-0.02 ± 0.03	-0.65	Xu et al. (2013)
G097.53+03.18	0.177±0.028	0.133±0.017	0.04 ± 0.03	1.34	Hachisuka et al. (2015)
IRAS 21379+5106	0.262±0.031	0.206±0.007	0.06 ± 0.03	1.76	Choi et al. (2014)
AFGL 2789	0.326±0.031	0.253±0.024	0.07 ± 0.04	1.86	Choi et al. (2014) ^a , Sakai et al. (2019)

^a If there are multiple references, we refer to papers labeled with *a* reporting higher accuracy parallaxes.

Table 3. Estimated Galactic parameters

Parameter	Power-law model		2nd-order polynomial model	
	Present study	Honma et al. (2012) ID14	Present study	Honma et al. (2012) ID22
R_0 (kpc)	7.92 ± 0.16	7.82 ± 0.41	7.97 ± 0.15	7.70 ± 0.40
Ω_0 (km s $^{-1}$ kpc $^{-1}$)	28.63 ± 0.26	29.60 ± 0.74	28.64 ± 0.26	29.71 ± 0.71
U_s (km s $^{-1}$)	4.2 ± 1.0	0.8 ± 1.4	4.3 ± 1.0	0.7 ± 1.4
V_s (km s $^{-1}$)	-4.9 ± 0.9	-6.3 ± 1.2	-3.7 ± 1.0	-6.5 ± 1.3
W_s (km s $^{-1}$)	-0.4 ± 0.7	-1.9 ± 1.1	-0.4 ± 0.7	-1.9 ± 1.1
α	-0.016 ± 0.012	0.00 ± 0.02	—	—
a_0 (km s $^{-1}$ kpc $^{-1}$)	—	—	-0.5 ± 0.4	-0.1 ± 0.7
b_0 (km s $^{-1}$ kpc $^{-2}$)	—	—	-0.2 ± 0.1	0.1 ± 0.2

Table 4. Comparison of Galactic center distance R_0

Method	Reference	R_0 (kpc)
VLBI astrometry of 188 maser sources	Present work	$7.92 \pm 0.16_{\text{stat.}} \pm 0.3_{\text{sys.}}$
VLBI astrometry of 147 maser sources	Reid et al. (2019)	8.15 ± 0.15
Orbital motion of S2 around Sgr A*	Gravity Collaboration et al. (2019)	$8.178 \pm 0.013_{\text{stat.}} \pm 0.022_{\text{sys.}}$
Orbital motions of S0-2 around Sgr A*	Do et al. (2019)	$7.946 \pm 0.050_{\text{stat.}} \pm 0.032_{\text{sys.}}$

Table 5. Comparison of angular velocity of the Sun Ω_\odot

Method	Reference	Ω_\odot (km s $^{-1}$ kpc $^{-1}$)
VLBI astrometry of 188 maser sources	Present work	$30.17 \pm 0.27_{\text{stat.}} \pm 0.3_{\text{sys.}}$
VLBI astrometry of 147 maser sources	Reid et al. (2019)	30.32 ± 0.27
Proper motion of Sgr A*	Reid & Brunthaler (2020)	30.39 ± 0.04